iScience

CellPress

Article

Two NEMO-like Ubiquitin-Binding Domains in CEP55 Differently Regulate Cytokinesis

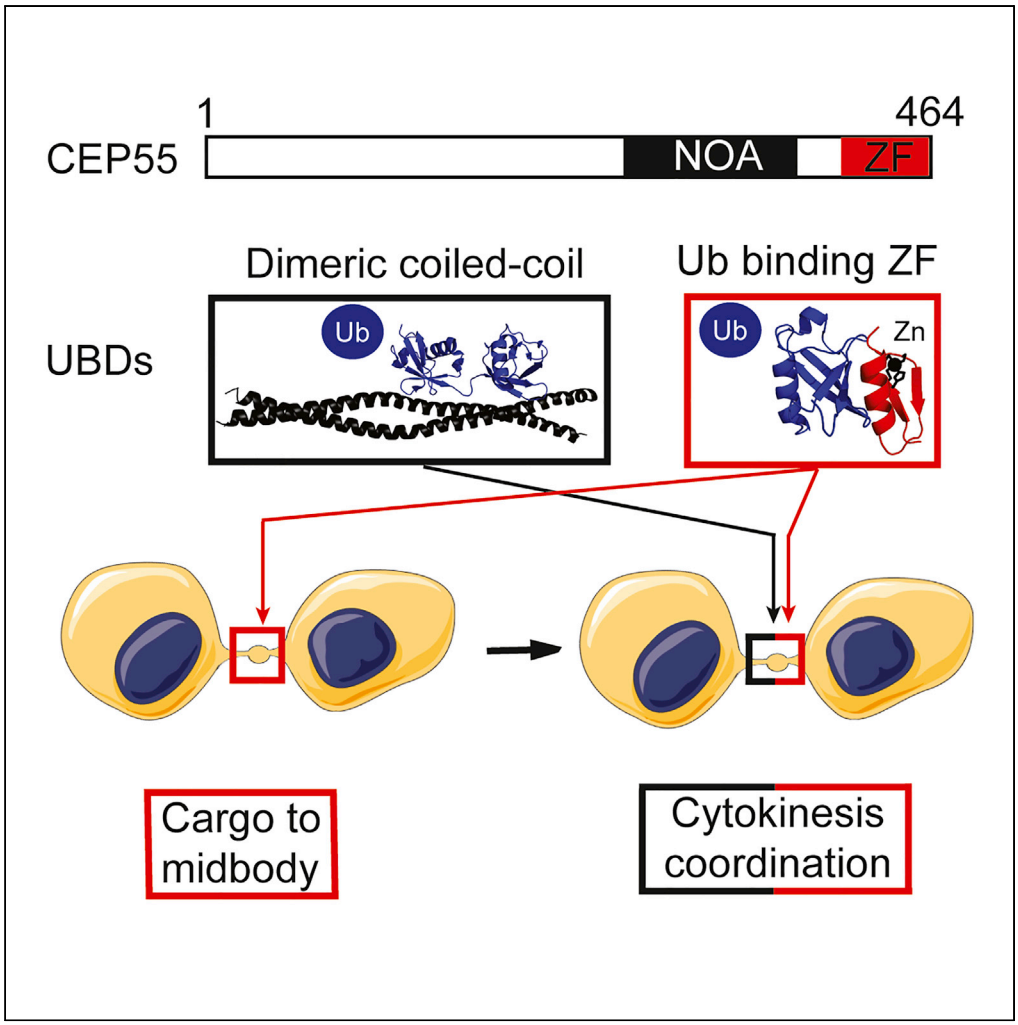

Keïs Nabhane Said Halidi, Elisabeth Fontan, Alix Boucharlat, ..., Alain Israël, Emmanuel Laplantine, Fabrice Agou

emmanuel.laplantine@upmc.fr (E.L.)
fabrice.agou@pasteur.fr (F.A.)

HIGHLIGHTS

CEP55 contains two NEMO-like NOA and UBZ domains

CEP55 NOA and UBZ are crucial for the CEP55 function in cytokinetic coordination

UBZ^{CEP55} functions as cargo receptor to the midbody in a ubiquitin-dependent manner

UBZ^{CEP55} preferentially binds non-degradative linear and K63 polyubiquitin chains

Said Halidi et al., iScience *20*, 292–309
October 25, 2019
https://doi.org/10.1016/j.isci.2019.08.042

iScience

CellPress

Article

Two NEMO-like Ubiquitin-Binding Domains in CEP55 Differently Regulate Cytokinesis

Keïs Nabhane Said Halidi,[1,4] Elisabeth Fontan,[1] Alix Boucharlat,[1] Laurianne Davignon,[1] Marine Charpentier,[1] Mikaël Boullé,[1,5] Robert Weil,[2,6] Alain Israël,[3] Emmanuel Laplantine,[2,6,7,*] and Fabrice Agou[1,7,8,*]

SUMMARY

CEP55 regulates the final critical step of cell division termed cytokinetic abscission. We report herein that CEP55 contains two NEMO-like ubiquitin-binding domains (UBDs), NOA and ZF, which regulate its function in a different manner. *In vitro* studies of isolated domains showed that NOA adopts a dimeric coiled-coil structure, whereas ZF is based on a UBZ scaffold. Strikingly, CEP55 knocked-down HeLa cells reconstituted with the full-length CEP55 ubiquitin-binding defective mutants, containing structure-guided mutations either in NOA^{CEP55} or ZF^{CEP55} domains, display severe abscission defects. In addition, the ZF^{CEP55} can be functionally replaced by some ZF-based UBDs belonging to the UBZ family, indicating that the essential function of ZF^{CEP55} is to act as ubiquitin receptor. Our work reveals an unexpected role of CEP55 in non-degradative ubiquitin signaling during cytokinetic abscission and provides a molecular basis as to how CEP55 mutations can lead to neurological disorders such as the MARCH syndrome.

INTRODUCTION

In animal cells, cytokinesis leads to the separation of the cytoplasm into two daughter cells. Defects during this process can lead to polyploidy and aneuploidy, situations that are frequently observed in cancers (Ganem et al., 2007). Cytokinesis begins in anaphase with the formation of an actomyosin ring, which constricts the plasma membrane of the cells, finally leading to the formation of an intercellular bridge (Mierzwa and Gerlich, 2014). Future daughter cells are connected by this intercellular bridge for several hours before individual assortment by a process termed abscission, which generally occurs in the G1 phase of the cell cycle (Gershony et al., 2014). At the center of the intercellular bridge is the midbody, a crucial component of the abscission process. It plays a role as the recruitment platform for abscission and acts as a stabilizer of the intercellular bridge (Mierzwa and Gerlich, 2014). After abscission, the midbody remnant (MR) is asymmetrically inherited by one of the two daughters cells and then degraded by autophagic or non-autophagic lysosomal pathways (Chen et al., 2013; Crowell et al., 2014).

Centrosomal protein 55 kDa (CEP55) is a key regulator of cytokinetic abscission. This protein is predominantly an α-helical coiled-coil protein, which is able to oligomerize (Zhao et al., 2006; Carlton and Martin-Serrano, 2007; Morita et al., 2007; Fabbro et al., 2005). CEP55 is essential for the recruitment of the Endosomal sorting complex required for the transport (ESCRT) machinery to the intercellular bridge (Morita et al., 2007; Carlton and Martin-Serrano, 2007; Carlton et al., 2008; Lee et al., 2008). CEP55 directly interacts with two components of the ESCRT machinery, ALG-2 interacting protein X (ALIX) and the ESCRT-I Tumor susceptibility gene 101 (TSG101), via its atypical α-helical coiled-coil dimeric region called EABR (ESCRT- and ALIX-binding region). Once recruited at the midbody through CEP55, the ESCRT complex orchestrates membrane remodeling events leading to the physical separation of the two daughter cells. In addition to its function in cytokinesis, CEP55 has also a central role in the midbody integrity maintenance (Zhao et al., 2006) and in the MR degradation (Ettinger et al., 2011; Kuo et al., 2011).

CEP55 is recruited to the midbody in late mitosis (Bastos and Barr, 2010). This recruitment depends on the Mitotic kinesin-like protein 1 (MKLP-1), a component of the Centralspindlin complex, which has been shown to co-immuno-precipitate with CEP55 under endogenous conditions as well as in reticulocyte lysates after *in vitro* transcription/translation of both proteins (Zhao et al., 2006; Bastos and Barr, 2010). It has been reported that CEP55 become phosphorylated during mitosis on its S425 and S428 residues by Cyclin-dependent kinase 1 (Cdk1) and Extracellular signal-regulated kinase 2 (Erk2), whereas its S436 residue is phosphorylated by Polo-like kinase 1 (PLK1) (Fabbro et al., 2005; Bastos and Barr, 2010). The PLK1 phosphorylation prevents CEP55 early recruitment to the mitotic spindle and its accumulation to the

[1]Chemogenomic and Biological Screening Core Facility, C2RT, Departments of Cell Biology & Infection and of Structural Biology and Chemistry, Institut Pasteur, 25 rue du Dr. Roux, 75724 Paris CEDEX 15, France

[2]Signaling and Pathogenesis Laboratory, Department of Cell Biology & Infection, Institut Pasteur, C.N.R.S UMR 3691, 25 rue du Dr. Roux, 75724 Paris CEDEX 15, France

[3]Department of Cell Biology & Infection, Institut Pasteur, 75724 Paris CEDEX 15, France

[4]Sorbonne Université, Collège doctoral, 75005 Paris, France

[5]Université de Paris, Sorbonne Paris Cité, Paris, France

[6]Present address: Sorbonne Université, INSERM U1135, CNRS ERL 8255, Center d'Immunologie et des Maladies Infectieuses (CIMI-Paris), 75013 Paris, France

[7]These authors contributed equally

[8]Lead Contact

*Correspondence: emmanuel.laplantine@upmc.fr (E.L.), fabrice.agou@pasteur.fr (F.A.)

https://doi.org/10.1016/j.isci.2019.08.042

midbody, and its impairment leads to severe abscission defects and inhibition of the ESCRT machinery recruitment to the midbody (Bastos and Barr, 2010; Kamranvar et al., 2016). It has been proposed that PLK1 could indirectly interact with CEP55 via the formation of a quaternary complex, which involves Myotubularin-related proteins 3 and 4 (MTMR3 and MTMR4) (St-Denis et al., 2015). Both these myotubularins were shown to be important in the abscission process regulating CEP55 recruitment to the midbody (St-Denis et al., 2015). Importantly, a severe human embryonic pathology called MARCH (multinucleated neurons, anhydramnios, renal dysplasia, cerebellar hypoplasia, and hydranencephaly) was recently associated with a deletion of the last 40 amino acids in CEP55, leading to a severe defect of CEP55 recruitment to the midbody (Frosk et al., 2017).

The post-translational modification of proteins by mono-ubiquitin or poly-ubiquitin chains of variable length and/or different linkage types is involved in a vast range of cellular processes, including autophagy, DNA repair, protein turnover, and many signal transduction events such as the nuclear factor (NF)-κB signaling pathway (Komander and Rape, 2012). These chains of ubiquitin are specifically recognized by proteins that contain ubiquitin-binding domains (UBDs), allowing a large number of effector proteins to translate the modifications into specific outcomes. In the NF-κB cascade, NEMO (NF-κB Essential Modulator) contains two UBDs, which non-covalently bind to hybrid M1/K63 poly-ubiquitin chains to trigger the NF-κB activation (Emmerich et al., 2013). The NEMO UBD referred to as NOA/UBAN domain (also called NUB or CC2-LZ) forms a long parallel α-helical coiled-coil dimer, which selectively binds to a Methionine 1 (M1) di-ubiquitin chain (Rahighi et al., 2009). The second UBD is a classical CCHC-type zinc finger (ZF), which adopts a ββα fold and interacts with a weak preference to lysine 63 (K63) and M1 over lysine 48 (K48) poly-ubiquitin chains (Cordier et al., 2009; Ngadjeua et al., 2013).

During cytokinesis, the E2/E3 ubiquitin ligase BRUCE (BIR repeat containing ubiquitin-conjugating enzyme), the deubiquitinases USP8 (Ubiquitin specific peptidase 8), and AMSH (Associated molecule with the SH3-domain of STAM) were reported to be located at the midbody and play key roles in the cytokinetic abscission process (Pohl and Jentsch, 2008) (Mukai et al., 2008). However, despite an accumulation of mono-ubiquitin and different types of poly-ubiquitin chains at the midbody and intercellular bridge, little is known about the role of ubiquitin signaling during the abscission process (Pohl and Jentsch, 2008; Mukai et al., 2008; Matsumoto et al., 2010).

Here, we identified CEP55 as a member of the NEMO-related protein family. Indeed, we show that CEP55, like NEMO, contains two UBDs, namely, NOA and ZF, which differently regulate CEP55 functions. Both domains bind to poly-ubiquitin chains *in vitro*, but NOA is specifically involved in the abscission process, whereas we showed that ZF is critical for CEP55 recruitment to the midbody and is therefore crucial in CEP55 functions at the midbody. Altogether our data reveal a critical role for non-degradative ubiquitination linked to CEP55 function in the last steps of cell division.

RESULTS

CEP55 Contains Two Ubiquitin-Binding Domains, which Are Structurally Similar to NOA and ZF UBDs of NEMO

The NEMO function depends on two UBDs in its C-terminal part, referred to as the NOA/UBAN domain (Laplantine et al., 2009; Wagner et al., 2008) and the ZF domain (Cordier et al., 2009; Ngadjeua et al., 2013). The NOA domain forms a long parallel α-helical coiled-coil dimer (Rahighi et al., 2009), whereas the ZF domain exhibits an UBZ (Ubiquitin-binding zinc finger) architecture based on a classical ββα fold (Cordier et al., 2009). Multiple sequence alignments including analysis of protein sequence databases, combined with the Paircoil2 algorithm, predict that the CEP55 protein contains in its C-terminal part two UBDs. We refer to these as NOA (residues 304–396, 38% similarity) and ZF (residues 435–464, 47% similarity), respectively, owing to their significant homologies with the same domains in NEMO, Optineurin and ABIN2 (Figures 1A, S1A, and S1B). To test this hypothesis, we first expressed in *E.coli* and purified to homogeneity a His-tag version of the human CEP55 NOA fragment (residues 304–396) (Figure 1B inset). Circular dichroism spectrum analysis in the far-UV showed that CEP55 His-NOA exhibits a high α-helical content of 80%, compatible with an α-helical coiled-coil structure (Figure 1B). To non-ambiguously determine the oligomeric state of CEP55 His-NOA in solution, we performed size exclusion chromatography experiments coupled in line with multi-angle light scattering (SEC-MALS), and showed that CEP55 His-NOA behaves mainly as monomers and dimers, with a very small amount of higher-order oligomers (3% of hexamers, Figure 1C). Based on these biochemical experiments, we generated a structural model of

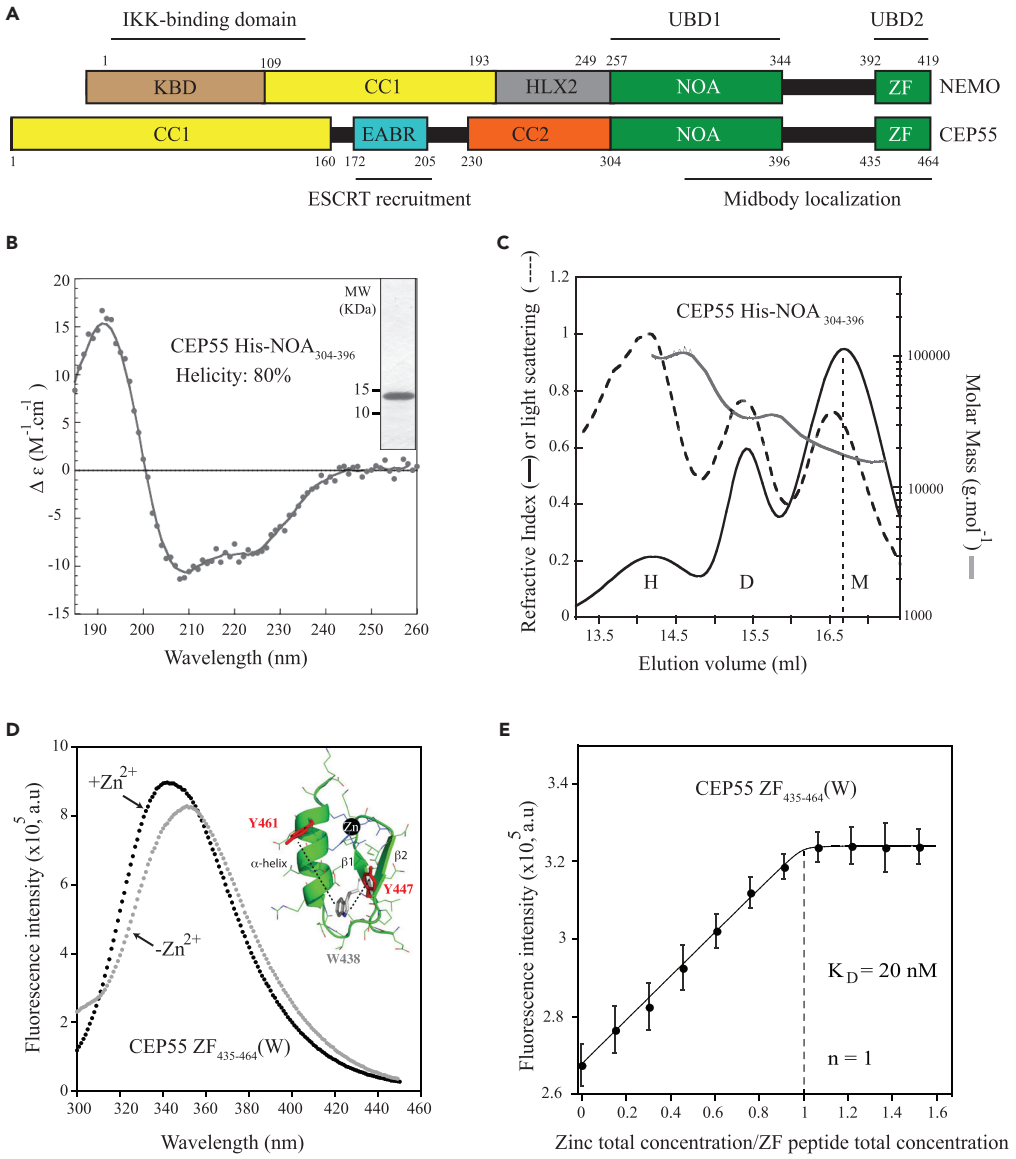

Figure 1. CEP55 Contains NOA and ZF Domains

(A) Schematic representation of structural and functional domains of CEP55 and NEMO showing a similar C-terminal architecture encompassing two ubiquitin-binding NOA and ZF domains. Sequence numbering is given for the human proteins (NP_001093327.1 and NP_001120654.1). KBD, Kinase binding domain; CC1-2, Coiled-coil 1 and 2; HLX2, Helical domain 2; EABR, ESCRT and ALIX binding region; NOA, NEMO, Optineurin and Abin domain (also called UBAN, CoZi, CC2-LZ and NUB); ZF, Zinc Finger; UBD, Ubiquitin-binding domain. Both EABR and NOA domains form parallel coiled-coil dimers.

(B) Normalized far-UV circular dichroism spectrum of purified CEP55 His-NOA (0.03 mg/mL at 1°C), showing a high α-helix content compatible with a coiled-coil structure. In inset is depicted the SDS-PAGE analysis of CEP55 His-NOA after staining with Coomassie blue.

(C) Analysis of CEP55 His-NOA by size exclusion chromatography coupled with multi-angle light scattering (SEC-MALS). M, Monomer; D, Dimer; H, Hexamer.

(D) Fluorescence emission spectra of CEP55 ZF V438W peptide (2 μM, hereafter denoted as ZF (W)) in the presence (black) or in absence of zinc ion (gray) after excitation of both tyrosine (Y447 and Y461) and tryptophan (W438) residues at 280 nm. Note that the emission shoulder peak observed in the 300–315 nm region, which is only observed in absence of zinc ion, reflects tyrosine fluorescence emission (Y447, Y461). This shoulder peak disappears and vanishes to the profit of tryptophan emission after ion zinc addition, owing to an increase of Tyr to Trp internal FRET. Inset: model of CEP55 ZF (W)

Figure 1. *Continued*
pointing out that the zinc-induced folding brings close together the two Y447, Y461 and W438 residues, leading to internal FRET.
(E) Fluorescence titration of CEP55 ZF (W) peptide (0.8 μM) using increasing zinc concentrations (0.1–1.4 μM) at excitation and emission wavelengths of 280 and 342 nm, respectively. Error bars represent the standard deviation of the fluorescence measurements of each titration point for 5 min.

the NOA^{CEP55} using NOA^{NEMO} as the structural template (Figure S1C) and observed that the C359 residue of one monomer is in close proximity with the C359 residue of the second monomer when NOA^{CEP55} forms an α-helical coiled-coil dimer (Figure S1E). We utilized this ability of the CEP55 His-NOA construct to form an intermolecular disulfide bond at C359 to further confirm its dimeric state. As shown in Figure S1F, CEP55 His-NOA migrated at the dimeric molecular mass in the absence of the reducing agent dithioerythritol (DTE), whereas it migrated at the monomeric molecular mass upon treatment with DTE, further confirming that CEP55 His-NOA likely forms a long parallel α-helical coiled-coil dimer like that of NEMO. However, this isolated NOA^{CEP55} domain appears to exhibit a much weaker dimerization affinity than that of NEMO NOA (6-fold less), which has been previously shown to have a dimerization constant around 30 μM (Hubeau et al., 2011).

To investigate whether the human CEP55 fragment containing the residues 435–464 adopts a zinc-finger fold, we generated a synthetic peptide mimicking this region and containing the V438W substitution (CEP55 ZF (W)). This substitution was previously described to act as a sensitive probe to monitor zinc-induced folding of the NEMO ZF without interfering with its overall structure (Cordier et al., 2009). We recorded the fluorescence emission spectrum of the CEP55 ZF (W) peptide at 300–450 nm using an excitation wavelength of 280 nm, allowing us to specifically irradiate the two tyrosines (Y447 and Y461) and tryptophan (W438) residues (Figure 1D). Upon zinc addition, CEP55 ZF (W) exhibits an increase of the fluorescence signal with a 7-nm blue shift of the tryptophan emission maximum (353–342 nm). Concomitantly, this leads to a decrease of the minor shoulder at 300–310 nm, which usually corresponds to fluorescence emission spectra of tyrosine residues. This clearly indicated that an internal FRET from tyrosine to tryptophan occurs only after the addition of zinc. In the presence and absence of zinc, the internal FRET efficiencies from Y to W were then determined and a 1.9 ± 0.06-fold increase was observed upon zinc addition (Table S1). Because internal FRET efficiency is highly sensitive to the distance between the acceptor and the donor, these data clearly indicated that zinc induces a spatial confinement of the two Y447 and Y461 to W438, reflecting a proper folding of the domain as a zinc finger. We took advantage of this zinc-dependent fluorescence signal at 342 nm to titrate CEP55 ZF (W) by zinc ion (Figure 1E). A strong binding affinity less than 20 nM was observed with a binding stoichiometry of 1:1. This binding stoichiometry was further confirmed using a colorimetric assay as described in Transparent Methods. Altogether, these data combined with multiple sequence alignment showed that the CEP55 fragment containing the residues 435–464 forms a CCHC-type ZF structure, which is likely built on a ββα fold. In a similar way to NOA^{CEP55}, a structural model of ZF^{CEP55} was generated using NEMO ZF as template, emphasizing the four residues (C440, C443, H458, and C462) that tetra-coordinate the zinc atom (Figure S1D) and that are strictly conserved among all CEP55 orthologues (Figure S1A).

NOA^{CEP55} Preferentially Binds to Linear Di-ubiquitin Chain, whereas ZF^{CEP55} Binds to Non-degradative Linear and K63 Chains

To assess the ability of CEP55 His-NOA to bind to poly-ubiquitin chains, we next performed qualitative Ni-NTA pull-down experiments in the presence of increasing concentrations of purified K63- and M1-linked tetra-ubiquitin (Ub_4) chains (Figures 2A and 2B). As negative control, we used a His-tagged recombinant protein (His-DARPin labeled Ctrl), which does not bind to any mono or poly-ubiquitin chains even at high concentration (up to 10 mM ubiquitin site concentration). As shown in Figures 2A and 2B, a specific binding of CEP55 His-NOA to K63- and M1-Ub_4 was observed in a dose-dependent manner. Interestingly, similar pull-down experiments using different ubiquitin linkage types revealed that CEP55 NOA preferentially recognizes non-degradative M1 and K63-linked Ub_4 chains over degradative K48- and K11-linked Ub_4 chains (Figure 2C), indicating that CEP55 His-NOA prefers to interact with open and even extended conformations of Ub_4. These results were surprising since the isolated NOA/UBAN domain of NEMO as well as its NEMO-related proteins OPTN and ABIN2 were reported to exhibit a strong linkage specificity for short M1 over K63 di-ubiquitin chains (Rahighi et al., 2009; Nakazawa et al., 2016; Lin et al., 2017). A possible explanation could be that pull-down experiments are only qualitative and performed under non-equilibrium conditions. For this reason, we next characterized

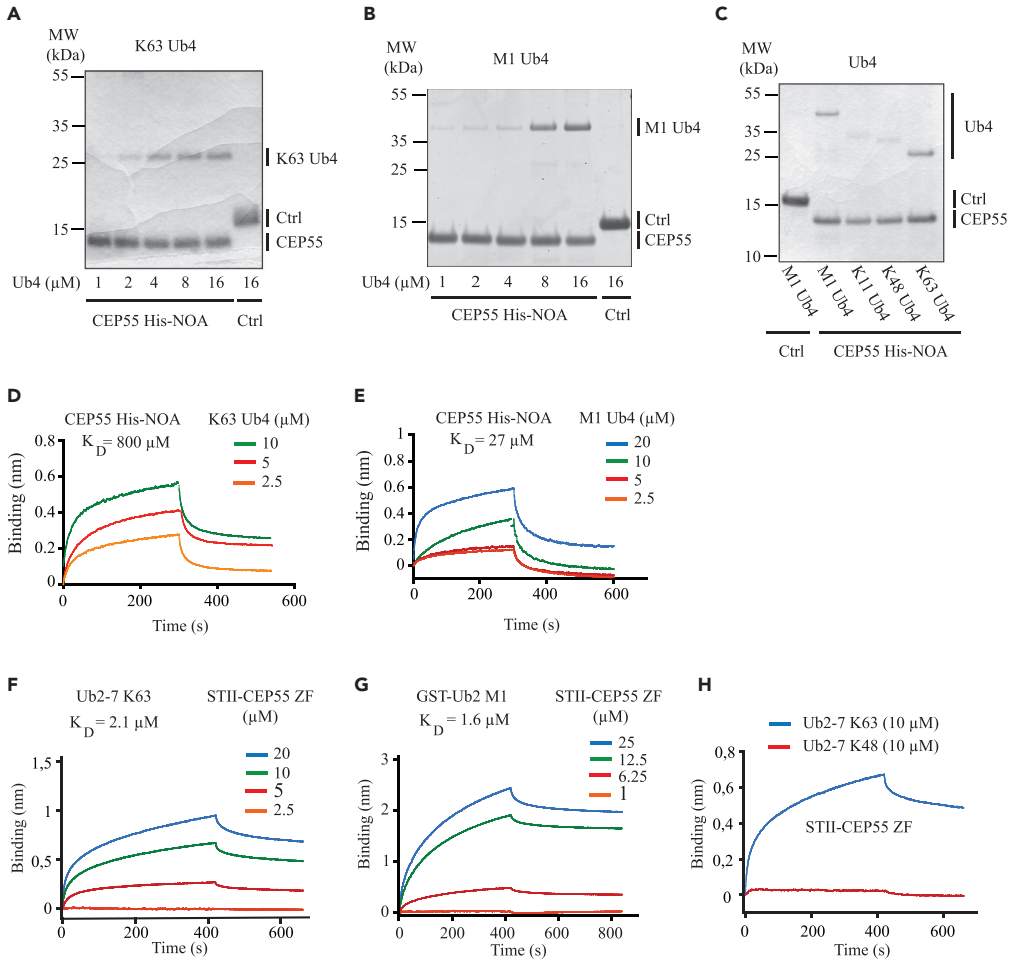

Figure 2. CEP55 NOA and ZF Form Specific Ubiquitin-Binding Domains, which Preferentially Bind to Non-degradative K63 and M1 Polyubiquitin Chains

(A and B) His pull-down experiments of CEP55 His-NOA (8 μM) with increasing concentrations of purified (A) K63 tetra-ubiquitin and (B) linear tetra-ubiquitin (1, 2, 4, 8, and 16 μM). Ctrl, negative control (His-DARPin).

(C) His pull-down experiment of CEP55 His-NOA (8 μM) with different linkages of tetra-ubiquitin chains (16 μM), including M1 (linear), K11, K48, or K63 tetra-ubiquitin as indicated. Ctrl, negative control (His-DARPin).

(D and E) Quantitative ubiquitin binding of CEP55 His-NOA by BioLayer Interferometry (BLI) using various concentrations of K63 (D) or linear (E) tetra-ubiquitin chains (2.5, 5, 10, and 20 μM). Anti-penta-His biosensors were used in each binding experiment to immobilize 8 μM of His-NOA (see Transparent Methods).

(F) Quantitative ubiquitin binding of Strep-tag II CEP55 ZF by BLI with a mixture of K63 Ub_{2-7} polyubiquitin chains. Biotinylated K63 Ub_{2-7} (0.2 mg/mL) was immobilized on a streptavidin biosensor before adding various concentrations of Strep-tag II CEP55 ZF (2.5, 5, 10, or 20 μM).

(G) Quantitative ubiquitin binding of Strep-tag II CEP55 ZF by BLI with an M1 (linear) di ubiquitin chain. M1 GST-Ub_2 (20 μM) was immobilized on an anti-GST biosensor before the addition of Strep-tag II CEP55 ZF at different concentrations (1, 6.25, 12.5, or 25 μM).

(H) Binding comparison of the Strep-tag II CEP55 ZF (10 μM) by BLI between a mixture of K63-Ub_{2-7} or K48 Ub_{2-7} polyubiquitin chains (0.2 mg/mL). For the experiments shown in (F)–(H), the Strep-tag II CEP55 ZF was each time freshly prefolded with 1 mM $ZnCl_2$, which was maintained at the same concentration in the binding buffer.

the interaction between CEP55 His-NOA and K63- or M1-Ub_4 chains by determining association (kon) and dissociation (koff) rate constants using biolayer interferometry (BLI) technology (Figures 2D and 2E). In this experiment, CEP55 His-NOA was first immobilized on anti-penta-His biosensors and incubated with different concentrations of K63- or M1-Ub_4. A K_D value of 27 μM for M1-linked Ub_4 chains was observed (Figure 2E), which is 30-fold lower than that of K63-linked Ub_4 (Figure 2D), indicating that CEP55 NOA preferentially binds to M1 poly-ubiquitin chains *in vitro*.

In a similar way, we next characterized the ability of CEP55 ZF to bind to K63 and M1 poly-ubiquitin chains using BLI assays. A mixture of biotinylated K63 poly-ubiquitin chains (Ub_{2-7}) and GST-Ub_2 M1 were immobilized on streptavidin (Figure 2F) and anti-GST antibody (Figure 2G) biosensors, respectively, before being incubated with increasing concentrations of a StrepII-tag version of CEP55 ZF peptides (STII-CEP55 ZF). CEP55 ZF similarly binds K63 Ub_{2-7} poly-ubiquitin chains and GST-Ub_2 M1, since similar K_D values of 2.1 and 1.6 μM were obtained, respectively. This ubiquitin-binding activity was specific because no binding was observed with a mixture of biotinylated K48 Ub_{2-7} chains (Figure 2H), indicating that CEP55 ZF preferentially recognizes K63 and M1 chains over K48 poly-ubiquitin chains. We also confirmed the specific binding of CEP55 ZF to mono- and K63 di-ubiquitin in solution by fluorescence polarization (FP) experiments using N-terminally fluorescein labeled CEP55 ZF and under more stringent buffer conditions (Figures S1G and S1H). Of note, similar binding affinities were observed with mono-ubiquitin and K63 di-ubiquitin in solution, but they were much lower than those obtained with BLI experiments. This is presumably because poly-ubiquitin chains were immobilized in BLI experiments, whereas they were in solution in FP experiments (see Discussion). Taken together, these data clearly demonstrated that CEP55 contains two UBDs in its C-terminal part: a UBZ-type (UBZ^{CEP55}) located at the C-terminal extremity that binds to non-degradative linear and K63 chains and an NOA domain (NOA^{CEP55}) that preferentially interacts with linear Ub chains.

Structure-Based Identification of UBZ^{CEP55} Mutants Defective in Ubiquitin Binding

Generation of ubiquitin binding defective single-point mutants of UBZ^{CEP55}, without altering the overall ZF structure, could be a challenging task since recent crystal complexes of UBZ domains with ubiquitin revealed different modes of ubiquitin recognition (Figure S2). Nevertheless, we could classify at least three groups of UBZ domains, including FAAP20/Polη (Toma et al., 2015; PDB:3WWQ [Bomar et al., 2007]), RAD18/WRNIP1 (Hu et al., 2017; PDB:5VF0 [Suzuki et al., 2016], PDB:3VHT), and NDP52 (Xie et al., 2015; PDB:4XKL), based on their crystal structures in complex with Ub (Figures S2A and S2B). Structure-based sequence alignment analysis of UBZ^{CEP55} from different organisms with different UBZ groups showed that UBZ^{CEP55} displays the highest homology with the RAD18/WRINP1 UBZ group, suggesting a similar ubiquitin-binding mode (Figure S2C). In particular, Ub-interacting residues of WRINP1-UBZ in the β1-strand, β-loop (the loop between both antiparallel β-strands), and the α-helix of the UBZ ββα fold are conserved or replaced by functionally equivalent residues in CEP55-UBZ (Figure S2C). These residues are also strictly conserved in CEP55 from several organisms. We therefore generated a structural model of CEP55 ZF in complex with ubiquitin, using the crystal structure of the UBZ-GFPWRNIP1:ubiquitin complex as template (Figure 3). According to this model, the CEP55 residue E460, which is strictly conserved among all CEP55 orthologues (Figure S1A), forms a strong binding determinant of the complex by making a dual salt bridge with R42 and R72 of ubiquitin (Figure 3A). To validate our hypothesis, we generated an N-terminally fluorescein-labeled CEP55 ZF mutant (F-ZF E460A) as well as a StrepII-tag version of CEP55 ZF mutant (STII-CEP55 ZF E460A) containing the E460A single point mutation. F-ZF E460A displayed an almost 20-fold weaker affinity compared with WT for mono-ubiquitin when determined in solution by FP (Figure 3B). We confirmed this drastic loss of affinity of the E460A mutant by BLI using immobilized GST-Ub2 M1, since binding affinity of the E460A UBZ mutant was 26-fold reduced compared with the WT (Figure 3C).

We then verified whether the E460A mutation impedes the ability of UBZ^{CEP55} to interact with ubiquitin and not the overall structure of UBZ domain. For this purpose, we investigated the zinc-induced folding of the E460A mutant (ZF^{CEP55} (W) E460A) by measuring its internal FRET efficiencies from tyrosine to tryptophan (Table S1). Similar fluorescence emission spectra of the WT and E460A mutant with or without the presence of Zn^{2+} indicated a similar folding (Figure S2D). Consistently, similar gains of internal FRET efficiencies from tyrosine to tryptophan were observed for the WT and E460A after the zinc addition (Table S1). Furthermore, Zn^{2+} titration experiments by fluorescence (Figure S2E) combined with a PAR colorimetric assay (data not shown) showed similar binding affinities and binding stoichiometries of the WT and E460A UBZ mutant. Thus, these data in agreement with our structural model indicated that the E460A mutation in UBZ^{CEP55} is a crucial binding determinant for ubiquitin recognition but does not alter the proper folding of this ZF structure.

CEP55 ZF and Its Ubiquitin-Binding Ability Are Necessary for CEP55 Recruitment to the Midbody

To study the functional role of UBZ^{CEP55} in the context of the full-length protein, we next carried out functional depletion/rescue experiments in HeLa cells. For this purpose, endogenous CEP55 was knocked

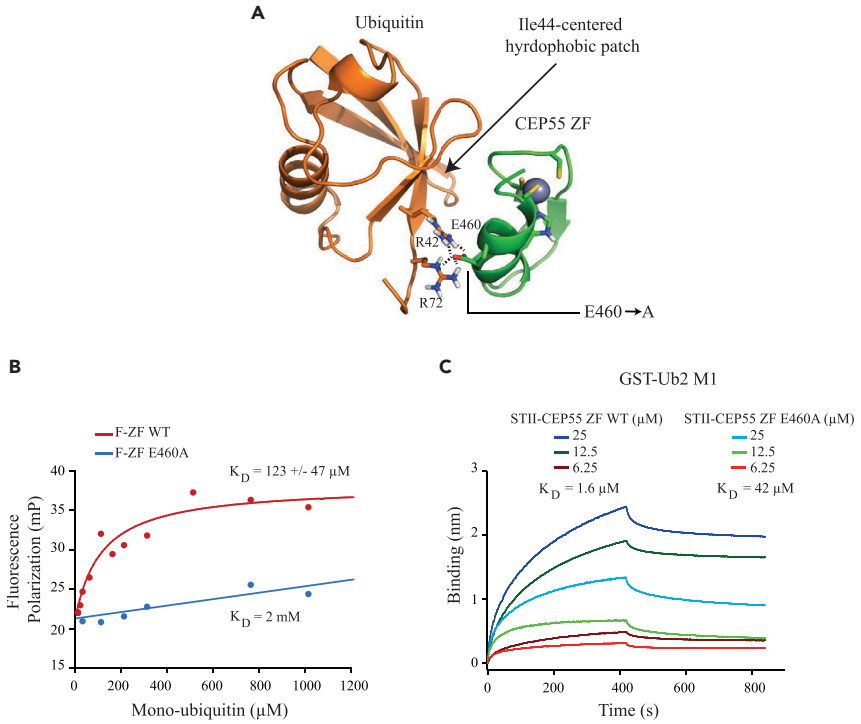

Figure 3. Structure-Based Identification of ZF Single-Point Mutant Defective in Ubiquitin Binding

(A) Structural model of CEP55 ZF (green) in complex with mono-ubiquitin (orange) pointing out E460 as a critical residue that makes a specific salt bridge with R42 and R72 residues of ubiquitin.

(B) Mono-ubiquitin titration in solution monitored by fluorescence polarization of fluorescein-labeled WT and E460A mutant CEP55 ZF (10 μM) in the presence of 1 mM $ZnCl_2$.

(C) Quantitative ubiquitin binding determined by BLI experiment of WT and E460A mutant CEP55 ZF with M1 (linear) di-ubiquitin chain. M1 GST-Ub2 was first immobilized on an anti-GST biosensor before adding various concentrations of WT and E460A mutant STII-CEP55 ZF (6.25, 12.5, and 25 μM). For the experiments shown in (B) and (C), all ZF peptides were freshly prefolded in the presence of 1 mM $ZnCl_2$, which was maintained at the same concentration in the binding buffer.

down by small interfering RNA (siRNA) and transiently re-expressed with siRNA-resistant plasmids expressing either CEP55 WT (HA-CEP55 WT), a debilitating double mutant (HA-C440A/C443A), which is unable to tetracoordinate the zinc atom, or the E460A single-point mutant defective in the ubiquitin binding (HA-CEP55 E460A). As shown in Figure 4A, knockdown of the endogenous CEP55 by siRNA was very efficient, and ectopic expressions of the WT and its single and double mutants gave similar expression levels of CEP55 as judged by western blot. As previously reported in the literature, efficient knockdown of CEP55 leads to an increase of cells connected by an intercellular bridge (Figures 4A and S3A) as well as multinucleated cells (Figures 4B and S3A). These phenotypes were partially restored by the expression of the HA-CEP55 WT protein (Figures 4A, 4B, and S3A). We do believe that the incomplete rescue was due to technical issues of simultaneously reaching very high transfections efficiencies with both DNA and siRNA and to intrinsic properties of the CEP55 protein, which lead to mainly insoluble protein under transient expression conditions, as previously described (Kuo et al., 2011) (Figure S3C). In addition, it is likely that the insoluble form of CEP55 could trap the soluble and functional form of CEP55 and so contributes to an incomplete rescue. Nevertheless, this rescue was statistically significant and reproducible (n = 3 with more than 300 nuclei/cells analyzed by experiment) (Figures 4A and 4B). Strikingly, neither the CEP55 C440A/C443A double mutant nor the CEP55 E460A single-point mutant were able to functionally rescue normal cytokinesis as does the WT, as judged by the persistent increase of cells connected by intracellular bridges (Figure 4A) and the increase in the proportion of multinucleated cells (Figure 4B) induced by CEP55 knockdown. These data clearly indicated that CEP55 ZF and its ubiquitin-binding property are crucial for CEP55 function during abscission. Moreover, the C440A/C443A double mutant and the E460A single-point mutant, unlike the WT, were unable to functionally restore the accumulation of MRs induced by CEP55 depletion (Figure S3B), highlighting a critical role of UBZ^{CEP55} in remnant midbody clearance.

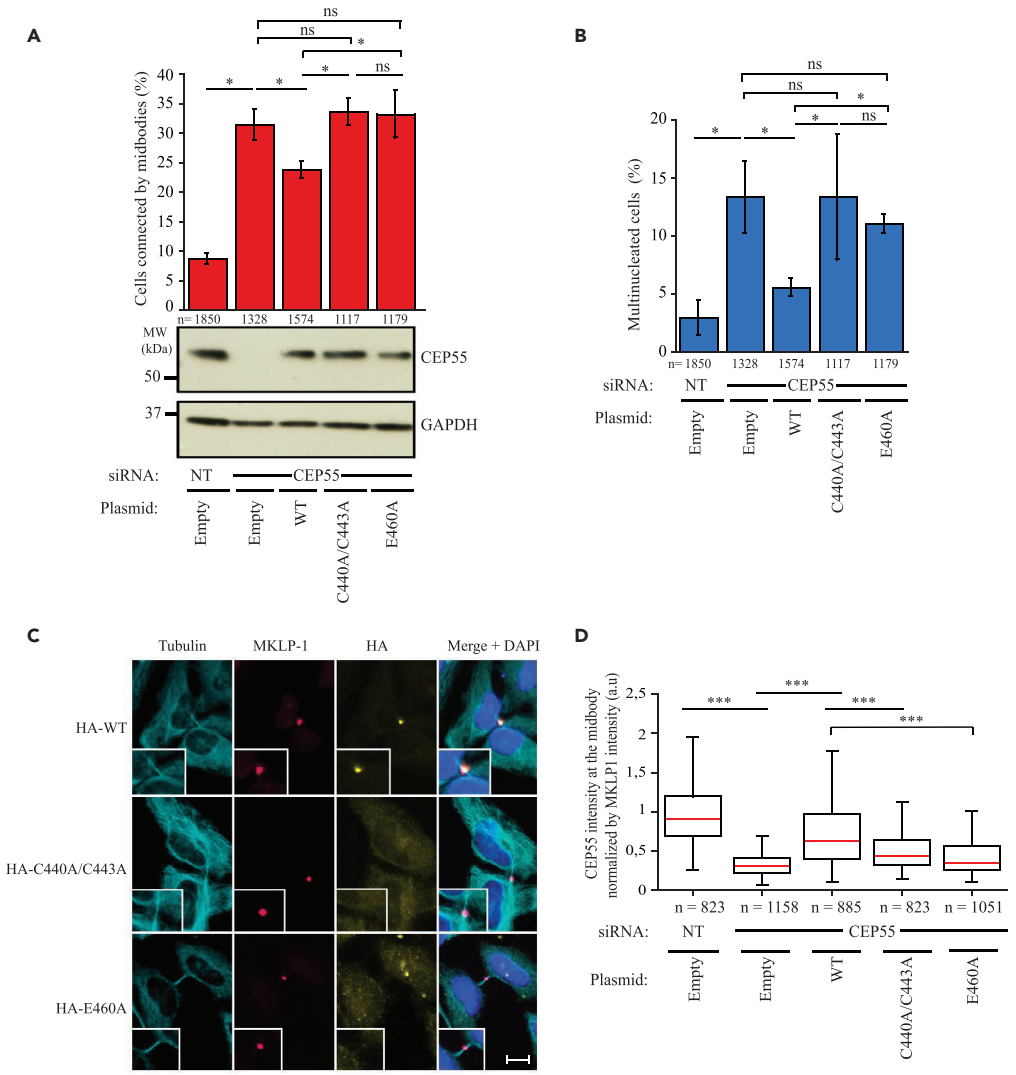

Figure 4. CEP55 ZF Is Essential for CEP55 Recruitment to the Midbody and Ensuring Proper Cytokinetic Abscission

HeLa cells were concomitantly transfected with a non-targeting (NT) or CEP55 siRNA and with an empty vector or a CEP55 siRNA-resistant vector encoding HA-CEP55 WT, HA-CEP55 C440A/C443A, or HA-CEP55 E460A.

(A and B) Analyses of the ZF mutant's ability to rescue cytokinesis defect induced by CEP55 depletion. The percentage of cells connected by midbodies (A) and the percentage of multinucleated cells (B) were quantified. Images are represented in Figure S3A. Data represent the mean ± SD of three independent experiments, and the total number of nuclei (n) counted in the three experiments is indicated. The level of expression of CEP55 in the soluble fraction for the different conditions was controlled by WB.

(C) Recruitment to the midbody of HA CEP55 WT, HA CEP55 C440A/C443A, and HA CEP55 E460A. Cells were stained with DAPI (blue) and immunolabeled with HA (yellow), MKLP-1 (red), and α-tubulin (cyan) antibodies. Insets show an expanded view of the midbody.

(D) Relative quantification of CEP55 intensity at the midbody reporter in the different conditions. Cells were stained with DAPI, CEP55, MKLP-1, and β-tubulin antibodies. CEP55 intensity was normalized by MKLP-1 intensity at each detected midbody (MKLP-1 spot).

Analyses were conducted on three independent experiments, n represents the total number of midbodies. Scale bar, 10 μM. ***$p < 0.001$; *$p < 0.05$; ns, not significant ($p \geq 0.05$).

Next, we assessed whether UBZ^{CEP55} could be involved in the recruitment of CEP55 to the midbody. Because transient expression of the ectopic CEP55 could interfere with the endogenous CEP55 via the formation of hetero-oligomers, similar functional knockdown and rescue experiments of endogenous CEP55 were performed.

Interestingly, although HA-CEP55 WT was recruited to the midbody, neither the C440/C443A double mutant nor the E460A single-point mutant were found to co-localize with the midbody (Figure 4C). Image quantification using MKLP-1 as midbody reporter confirmed the defect of both CEP55 mutants in their recruitment to the midbody compared with the WT (Figure 4D). In line with this, the ALIX endogenous protein, which is recruited to the midbody via CEP55 binding, also exhibited a clear defect in midbody localization with both CEP55 ZF mutants, but not the WT, using again MKLP-1 as midbody reporter (Figure S3D).

Taken together, these results reveal that the UBZ^{CEP55} UBD and its ubiquitin-binding properties are crucial for CEP55 recruitment to the midbody, allowing CEP55 to ensure proper abscission and MR clearance.

Structure-Based Identification of CEP55 NOA Mutants Unable to Bind Ubiquitin

The precise mode of linear di-ubiquitin recognition by the NOA/UBAN domain originally found in the NEMO protein (Rahighi et al., 2009) was more recently confirmed by two other NEMO-like proteins called Optineurin (Nakazawa et al., 2016) and ABIN2 (Lin et al., 2017). Indeed, structural comparison of NEMO NOA in complex with an M1-linked di-Ub with the recent crystal structures of Optineurin with a linear di-Ub chain (Nakazawa et al., 2016) and ABIN2 with a linear tri-Ub chain (Lin et al., 2017) revealed a highly conserved binding mode of NOA with two M1-linked units of ubiquitin (Figure S4). Contrary to the UBZ family, the NOA UBD forms a long parallel α-helical coiled-coil dimer, in which one monomer mainly interacts with the distal Ub (second Ub), whereas the other monomer interacts with the proximal ubiquitin (first Ub). This explains why the NOA dimeric state is required for ubiquitin binding. Structure-based sequence alignment of NOA UBD family with CEP55 from different organisms reveal the presence of conserved or functionally equivalent ubiquitin-interacting residues with both proximal and distal ubiquitin. This sequence conservation suggests that CEP55 binds to a di-Ub chain in a similar manner to NOA family and the degree of conservation of each amino acid position was higher between CEP55 and ABIN2 NOA, especially when compared with residues interacting with proximal ubiquitin (Figure S4). We then generated a structural model of CEP55 NOA in complex with a linear di-Ub chain using the linear diubiquitin:NOA complex of NEMO as structural template (PDB: 2ZVO) (Figure 5A). According to the model, L351, Q354, and Q355 interact with the I44 centered hydrophobic patch of the distal ubiquitin (Figure 5A, left panel). L351 and Q355 residues are perfectly conserved in all the NOA family and CEP55 orthologs, whereas Q354 is conserved only in ABIN2. Moreover, D362 and F363 interact with the C-terminal tail of distal ubiquitin and are strictly conserved in all the NOA family (Figures 5A right panel and S4).

To validate the importance of these ubiquitin-interacting residues, we purified to homogeneity two His-NOA mutants containing either the L351A/Q354A/Q355A triple mutation or D362R/F363P double mutation and assessed their affinities with M1-linked tetra-ubiquitin by BLI (Figures 5B and S5A–S5C). A deletion mutant of the residues 343–364 corresponding to the minimal NOA site was also generated taking into account the nature of the heptad repeats in the coiled-coil dimer. For all of the three mutants, we observed drastic losses of binding affinity for M1-linked Ub_4 compared with the WT (more than 500-fold), indicating that the mutated residues within the double and triple mutants correspond to critical ubiquitin-binding determinants in agreement with our structural model. To determine whether these mutations also caused global disruption of the dimeric coiled-coil structure, we next analyzed the mutants by SDS-PAGE in the absence of the reducing agent DTE (Figure S5D) and by SEC-MALS (Figure S5E). The L351A/Q354A/Q355A triple mutant and the deletion mutant form considerably less stable dimers than the WT, as no dimers with both mutants were detected by SDS-PAGE in the absence of DTE and SEC-MALS. For the D362R/F363P double mutant, a significant amount of dimers could be detected in SDS-PAGE without DTE, indicating that this mutant forms more stable dimers than the triple and deletion mutants. Nevertheless, the D362R/F363P mutant dimer was less stable than the WT, as judged by the dimer/monomer ratio of the mutant in SDS-PAGE without DTE, which is significantly lower than the WT. Furthermore, no dimer with this mutant could be observed with SEC-MALS. Rather, we could detect a second form of monomer more compact, which likely results from the replacement of Phe363 by Pro363 in this mutant. Therefore, all structure-guided mutants generated from the structural model displayed a total loss of ubiquitin binding activity, but they also displayed a defect in dimerization properties to varying extents.

CEP55 NOA Is Absolutely Required for Normal Cytokinetic Abscission but Not for CEP55 and ALIX Recruitment to the Midbody

To investigate the functional importance of CEP55 NOA UBD, we carried out functional depletion/rescue experiments in HeLa cells. To this end, we generated the D362R/F363P double mutant in the context of the

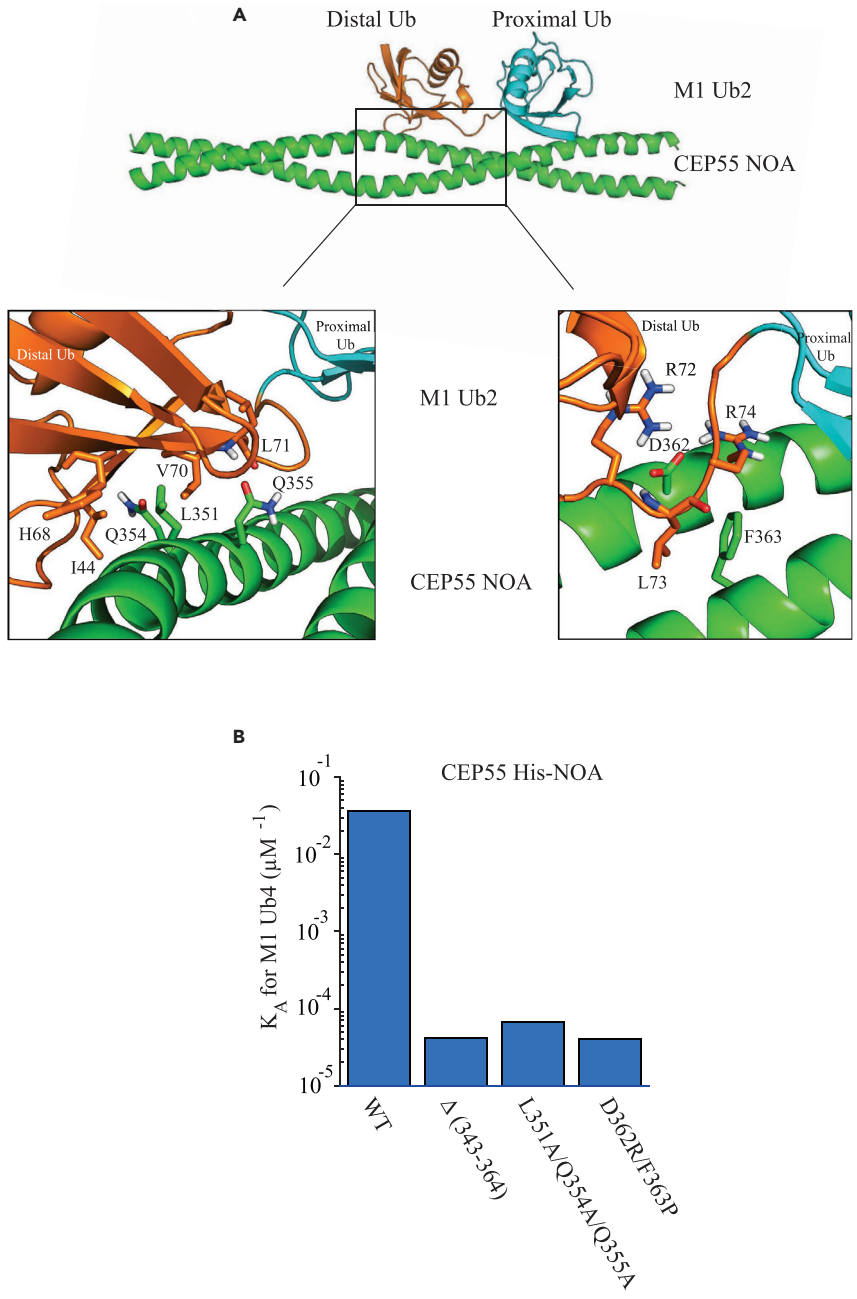

Figure 5. Structure-Based Identification of CEP55 NOA Mutants Defective in Ubiquitin Binding

(A) Modelization of CEP55 NOA (green) in interaction with linear di-ubiquitin pointing out critical residues in the recognition of the distal ubiquitin (orange) and proximal ubiquitin (cyan). Zoom on the interface between distal ubiquitin and CEP55 NOA. Left: residues involved in the recognition of the hydrophobic patch of the distal ubiquitin. Right: residues involved in the recognition of the C-terminal tail of the distal ubiquitin.

(B) Comparison of the association constants (K_A) of the different His-NOA mutants for linear tetra-ubiquitin measured by BLI. Curves are represented in Figures S5A–S5C.

full-length CEP55 protein. As shown in Figure 6A, the protein expression level of the D362R/F363P double mutant was similar to that of the WT. Nevertheless, it is worth noting that a significant portion of the WT and mutant proteins were found in the insoluble fraction of cell lysates, as we found for the CEP55 UBZ mutants (Figures S3C and S6C). Importantly, ectopic expression of the D362R/F363P double mutant was not able to rescue the cytokinetic defect induced by CEP55 knockdown, contrary to the WT (Figures 6A and S6A).

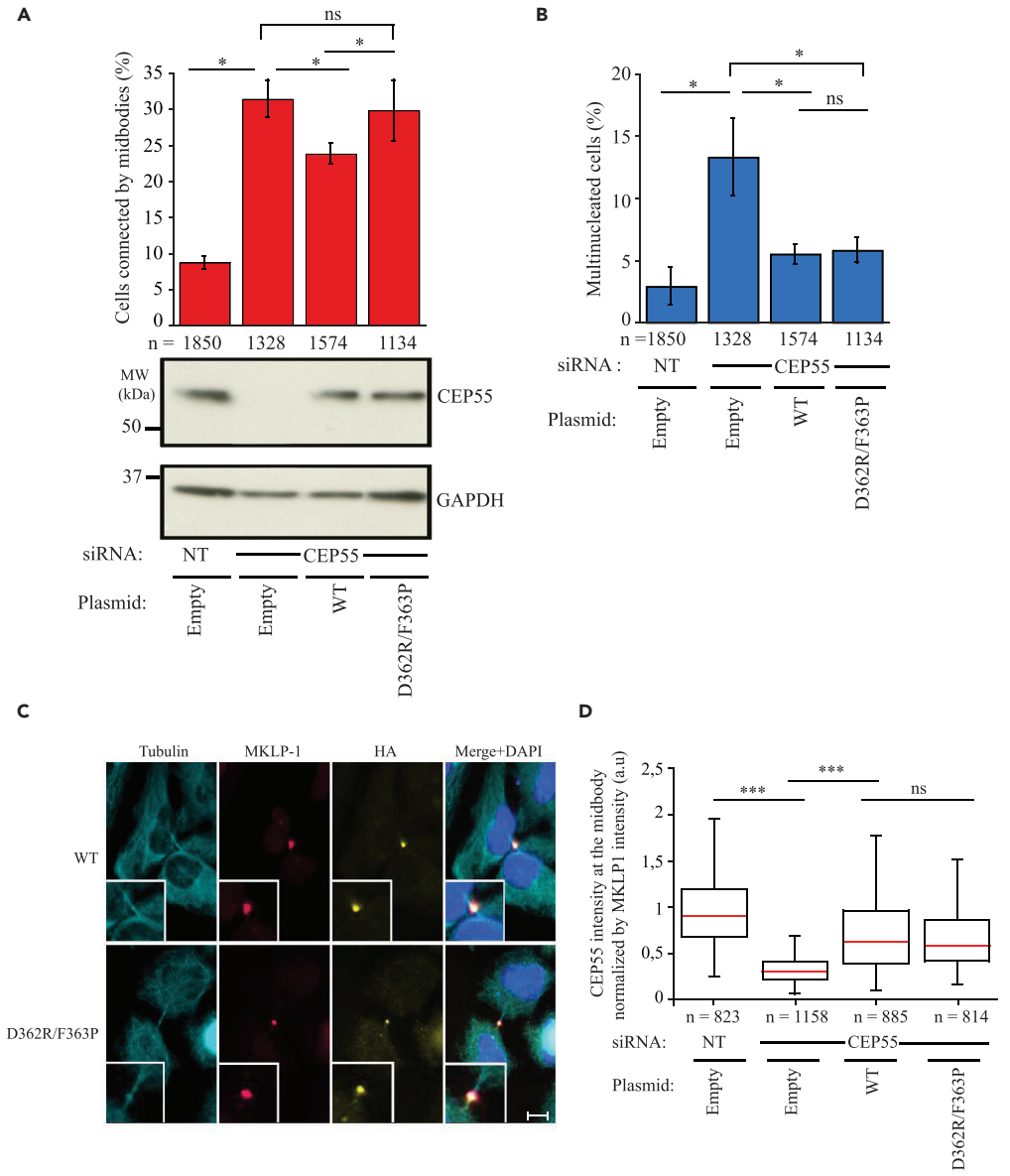

Figure 6. CEP55 NOA Is Not Involved in CEP55 Recruitment to the Midbody but Is Absolutely Required to Ensure Proper Abscission

(A and B) Effect of the double NOA mutant (D362R/F363P) on the ability to rescue cytokinesis defect induced by CEP55 depletion. HeLa cells were concomitantly transfected with a non-targeting (NT) or CEP55 siRNA and with an empty vector or a CEP55 siRNA-resistant vector encoding either HA-CEP55 WT or HA-CEP55 D362R/F363P. The percentage of cells connected by midbodies (A) and the percentage of multinucleated cells (B) were quantified. Representative images are shown in Figure S6A. Data represent the mean ± SD of three independent experiments, and the total number of nuclei (n) counted in the three experiments is indicated. The level of CEP55 expression in the soluble fraction were controlled by western blot as indicated.

(C) Recruitment to the midbody of HA-CEP55 WT and HA-CEP55 D362R/F363P. Same immunofluorescence experiments as (A). Cells were then stained with DAPI (blue) and immunolabeled with HA (yellow), MKLP-1 (red), and α-tubulin (cyan) antibodies. Insets show an expanded view of the midbody. Scale bar, 10 μM.

(D) Relative quantification of CEP55 intensity at the midbody as indicated. Immunofluorescence experiments were the same as (A) except for CEP55 labeling. CEP55 intensity was normalized by MKLP-1 intensity at the midbody upon MKLP-1 dots. The total numbers of midbodies (n) that result from three independent experiments are indicated.

***$p < 0.001$; *$p < 0.05$; ns, not significant ($p \geq 0.05$).

On the other hand, the amount of multinucleated cells was almost similar in cells expressing either the double mutant or the WT (Figures 6B and S6A). Although an increase of cells connected by an intercellular bridge may reflect a delay in the abscission process, the appearance of multinucleated cells often results from more drastic abscission defects and/or an earlier event involved in the stabilization of the intercellular bridge and midbody integrity. In the case of CEP55, previous studies showed CEP55 plays crucial roles in midbody integrity (Zhao et al., 2006; Carlton et al., 2008) as well as in the abscission process (Morita et al., 2007; Carlton and Martin-Serrano, 2007; Lee et al., 2008). Consistent with previous studies, we conclude that the CEP55 NOA UBD plays an important role in CEP55 during abscission, albeit to a lesser extent than UBZ^{CEP55}, and does not appear to be involved in the stabilization of the intercellular bridge or seems less important than CEP55 ZF in the abscission process.

Moreover, although the D362R/F363P double mutant exhibits a defect in the abscission process, it is normally recruited to the midbody, indicating that the detrimental effect of the mutant in cytokinesis occurs after its recruitment to the midbody (Figures 6C and 6D). Consistent with these data, we also observed that the D362R/F363P double mutant was able to recruit ALIX to the midbody as efficiently as the WT (Figure S6D), suggesting that the functionality of the EABR dimeric domain was not affected by the ubiquitin-binding deficient mutation in the NOA domain in the context of the full-length protein.

Finally, we quantified the percentage of the remnants by cell using knocked down HeLa cells of CEP55 expressing either the WT or the double mutant (Figure S6B). No difference was observed between the WT and the double mutant, indicating that CEP55 NOA is not involved in CEP55 MR clearance.

Altogether, our results showed that NOA UBD plays an important role in cytokinetic abscission, albeit to a lesser extent than UBZ^{Cep55} UBD, and is not involved in CEP55 nor in ALIX recruitment to the midbody neither in MR clearance.

UBZ^{CEP55} Functions as a Specific Targeting Domain to the Midbody in a Ubiquitin-Binding-Dependent Manner

We next focused our studies on the UBZ-dependent recruitment of CEP55 to the midbody by examining the possibility that this domain alone could serve as a specific midbody localization signal. If UBZ^{CEP55} forms an autonomous UBD domain for this targeting activity to the midbody, thus, any fusion proteins that only contain the UBZ^{CEP55} domain should be specifically recruited to the midbody. For this purpose, we generated a GFP-UBZ^{CEP55} construct and investigated by fluorescence microscopy its cellular localization. As shown in Figures 7A and 7B, GFP-UBZ^{CEP55}, but not GFP alone, co-localized with the midbody marker, MKLP-1, indicating that UBZ^{CEP55} exhibits a specific targeting activity to the midbody. This was not due to the differences of protein expression level because GFP and GFP-UBZ^{CEP55}were expressed as similar levels in cells (Figure 7C). Because endogenous CEP55 could interfere with the GFP-UBZ^{CEP55} recruitment to the midbody, we then performed experiments in CEP55 knock-downed HeLa cells, concomitantly expressing GFP alone or GFP-UBZ^{CEP55} (Figures S7A and S7B). No significant difference in the targeting activity was observed in cells transfected with an siRNA control and CEP55-specific siRNA, demonstrating that the endogenous CEP55 was not necessary for the recruitment of GFP-UBZ^{CEP55} to the midbody.

We next addressed the question whether this CEP55 UBZ-dependent targeting activity depends on its ability to bind to ubiquitin and whether this ubiquitin binding depends on one type of M1 or K63 linkage of polyubiquitin chains. For these experiments, we generated CRISPR-Cas9-mediated CEP55 knockout U2OS cell lines to increase the sensitivity of our functional complementation assay (Figure S7C). We also generated different CEP55 chimeric proteins in which the CEP55 UBZ was replaced with other classes of UBD based on small ZF modules known to interact with ubiquitin such as UBZ^{WRNP1}, UBZ^{RAD18}, UBZ^{NDP52}, $nZF2^{TAB2}$, and $A20^{ZF7}$ (Figure 7D). UBZ^{WRNP1} and UBZ^{RAD18} were chosen because their crystal structures showed a binding mode similar to that of ubiquitin, which is likely close to that of UBZ^{CEP55}. In addition, UBZ^{WRNP1} exhibits no ubiquitin linkage specificity, whereas UBZ^{RAD18} exhibits a little preference for K63 over K48 polyubiquitin (4-fold) and an *in vitro* stronger polyubiquitin binding, owing to the extended LR motif (224–240) located at its C terminus (Thach et al., 2015). We also used the UBZ^{NDP52}, which is also built on a $\beta\beta\alpha$ fold structurally related to UBZ^{WRNP1} and UBZ^{RAD18}. However, it uses a different mode of ubiquitin recognition (Figures S2B and S2C) and was reported to have no specificity for one type of ubiquitin linkage (Toma et al., 2015). By contrast, $nZF2^{TAB2}$ and $A20^{ZF7}$ display strong linkage specificity for K63 and M1

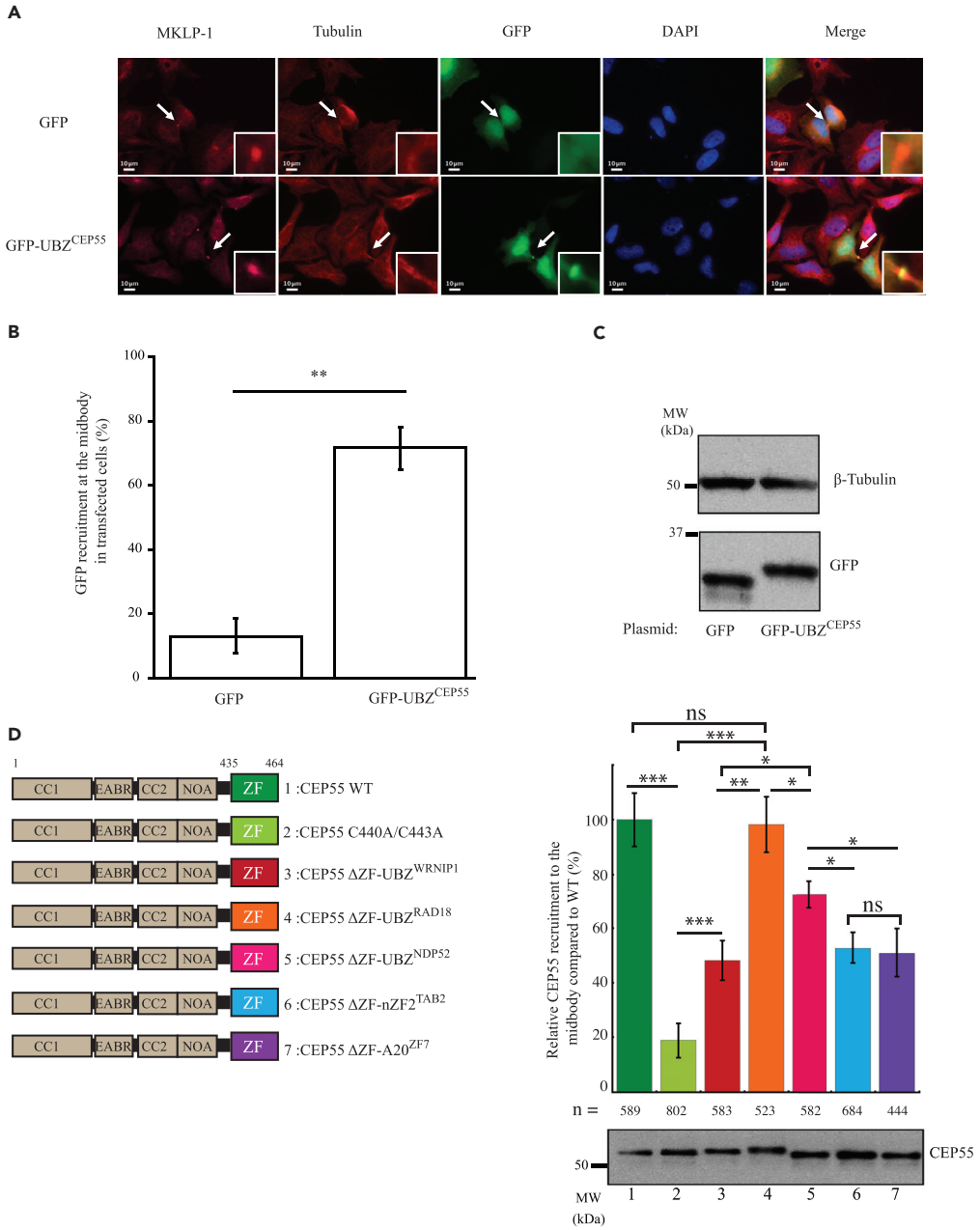

Figure 7. Ubiquitin-Binding Activity of CEP55 UBZ Is Required to Function as a Specific Cargo Receptor to the Midbody

(A) HeLa cells were transiently transfected with plasmids encoding for GFP alone or GFP-UBZ^{CEP55} and then analyzed by immunofluorescence and fluorescence microscopy.

(B) Quantification of the percentage of co-localization between GFP or GFP-UBZ^{CEP55} and MKLP-1 (midbody reporter) in transfected cells. Data represent the mean ± SD of six independent experiments. **p < 0.01.

(C) Expression levels were controlled by western blot.

(D) CRISPR-Cas9-mediated CEP55 knockout U2OS cell lines were transiently reconstituted following transfection with different plasmids encoding the WT, a debilitating double mutant unable to form a ZF structure (C440A/C443A), or the chimeric CEP55 proteins containing different ZF groups interacting with ubiquitin as indicated (left panel and Figure S2). Reconstituted cells were then analyzed by immunofluorescence and the levels of expression controlled by western blot

Figure 7. *Continued*

before quantifying the percentages of co-localization between CEP55 and MKLP-1 (midbody) for the indicated chimeric CEP55 proteins.

Data represent the mean ± SE of two independent experiments; n represents the total number of midbodies.

***p < 0.001; **p < 0.01; *p < 0.05; ns, not significant (p ≥ 0.05).

polyubiquitin chains, respectively, but they are likely structurally different from UBZ^{CEP55}. CEP55 knockout U2OS cells generated by the CRISPR-Cas9 technology were transiently reconstituted following transfection with different plasmids encoding for either the WT or the chimeric CEP55 proteins bearing the different UBZs mentioned before or a debilitating double mutant (C440A/C443A, unable to form a ZF structure). Reconstituted cells were then analyzed by immunofluorescence to quantify the percentages of co-localization between CEP55 and the midbody marker, MKLP-1. The level of expression of the different constructs was controlled by western blot in parallel experiments. As shown in Figure 7D, CEP55 ΔZF-UBZ^{RAD18} totally restored the CEP55 recruitment to the midbody, similar to the WT, whereas the debilitating double mutant did not. All chimeric CEP55 proteins were expressed at a similar level in U2OS cells. The four other chimeric CEP55 proteins, CEP55 ΔZF-UBZ^{NDP52}, ΔZF-UBZ^{WRNP1}, ΔZF-$nZF2^{TAB2}$, and ΔZF-$A20^{ZF7}$, also complement the targeting activity of CEP55 but to in a lesser extent than the WT. Nevertheless, the CEP55 ΔZF-UBZ^{NDP52} significantly displayed a better restoration than those of CEP55 ΔZF-UBZ^{WRNP1}, CEP55 ΔZF-$nZF2^{TAB2}$, and CEP55 ΔZF-$A20^{ZF7}$, which partially complement the CEP55 recruitment to the midbody at a similar level. Importantly, no significant difference was observed between CEP55 ΔZF-$nZF2^{TAB2}$ and CEP55 ΔZF-$A20^{ZF7}$, indicating that no predominant M1 or K63 linkage was required for the UBZ-dependent targeting activity of CEP55.

Next, we addressed the question of how the CEP55 UBZ contributes to cellular poly-Ub binding in the context of the full-length protein. To this end, His-tagged WT or mutant (C440/C443A) human full-length CEP55 purified from 293-F cells were incubated with whole-cell extracts containing free and anchored polyubiquitin chains. His-tagged WT and UBZ double mutant immobilized on Ni-NTA beads were then pulled down, and bound polyubiquitin chains were revealed by western blot using anti-Ub antibodies (Figure S7D). As negative control, we used a mutant of the NOA/UBAN ubiquitin binding domain of NEMO (D311G), which is defective in ubiquitin binding. We observed that the CEP55 UBZ significantly contributes to polyubiquitin binding since the C440A/C443A debilitating double mutant exhibits a slight, albeit significant decrease in polyubiquitin binding activity compared with the CEP55 WT. Note that this polyubiquitin binding activity of the UBZ double mutant was not totally abolished when compared with the NOA/UBAN mutant of NEMO. This suggests that CEP55 NOA, as well as the EABR domain, which interacts with UBD-containing ALIX and TSG101 proteins, could contribute to the polyubiquitin binding activity of CEP55. Moreover, and unsurprisingly, we observed that CEP55 and polyubiquitin chains specifically colocalize with each other and are localized to the midbody at the late stage of cytokinesis (Figure S7E).

Altogether, we conclude that the ubiquitin binding ability of CEP55 UBZ is required to specifically target the CEP55 protein to the midbody. In addition, no significant linkage preference for M1- or K63-linked chains was observed for this targeting activity, consistent with the ubiquitin-binding properties of CEP55 UBZ.

DISCUSSION

NEMO is the prototype of a family of proteins including Optineurin and ABIN2, which contain the same type of UBDs. Although the UBD of these proteins are conserved, they exert different functions such as NF-κB regulation in the case of NEMO, membrane trafficking and autophagy in the case of Optineurin, and NF-κB and ERK MAP kinase regulation in the case of ABIN2. Here we identified the CEP55 protein, a regulator of cytokinesis, as a member of this family protein, which contains both NOA/UBAN and UBZ domains in the C-terminal part of the protein. Although we did not determine the tridimensional structures of these UBDs, we showed strong evidences by structure-guided sequence alignment analysis and biochemical and biophysical experiments that the predicted CEP55 NOA fragment (residues 304–396) adopts an α-helical coiled-coil dimer and in the C-terminal region (residues 435–464) a ZF/UBZ architecture, which are structurally similar to those of NEMO, Optineurin, and ABIN2 proteins. Based on these experiments, we generated structural models of both CEP55 NOA and UBZ domains, which are fully consistent with mutagenesis data and allowed us to identify several mutants defective in ubiquitin binding. These generated mutants in each domain and in the context of the full-length protein also permitted the

demonstration of the functional importance of these NOA and UBZ domains for the CEP55 function in cell division and specifically in cytokinetic abscission.

Despite an extensive search of crystallization conditions and generation of different constructs, no high-quality diffraction crystals of CEP55 NOA or CEP55 UBZ with or without ubiquitin could be obtained. For NOA, this was likely due to its high tendency to form higher-order oligomers (mainly hexamers), which probably result from the assembly of three dimeric units. In the case of CEP55 UBZ, this was due to its poor solubility at high concentration as judged by dynamic light scattering experiments (data not shown). Moreover, this tendency of recombinant or synthetic CEP55 UBZ to aggregate and collapse when used at a concentration above 50–70 μM prevented us to determine its structure by NMR, contrary to NEMO UBZ for which we successfully solved the NMR structure (Cordier et al., 2009).

Although CEP55 NOA is structurally similar to NEMO and its related proteins, Optineurin and ABIN2, some characteristic features of CEP55 were observed. First, the nature of the typical seven-residue periodicity (abcdefg)n, known as the heptad repeat, significantly differs from that of NEMO in the N-terminal part of the NOA domain, also called the CC2 region in NEMO. Indeed, four hydrophobic residues at a and d heptad positions in NEMO (a: L260, L274 M295; d: A270), which are crucial for the dimer stability, are replaced by polar and charged residues in CEP55 (a: N311, S325, Q346; d: E321). The presence of these polar and charged residues could destabilize the hydrophobic packing of the α-helical coiled-coil dimer in the N-terminal region of CEP55 NOA, providing a possible explanation why the CEP55 NOA forms a dimer less stable than that of NEMO, with a dimerization constant that is about 6-fold lower than that of NEMO (Grubisha et al., 2010). In line with this, caution also should be taken on the apparent linkage selectivity for linear chains observed with the isolated NOA of CEP55. Indeed, previous crystal structures of NOA complexes with K63- and M1-linked di-ubiquitin chain revealed the interactions with the two ubiquitin moieties of M1-linked di-ubiquitin chain (distal and proximal), whereas only the distal ubiquitin moiety interacts with the K63-linked di-ubiquitin chain. These differences in ubiquitin-binding mode can lead to a more stabilizing effect on the NOA dimerization with the linear chain compared with K63 chains. Thus, the differences of affinity between linear and K63 chains for NOA CEP55 could be artificially enhanced by the dimerization effect induced by linear chain binding, possibly leading to an overestimation of linkage selectivity of CEP55 NOA for linear chains over K63 chains.

Even though size exclusion chromatography showed that the D362R/F363P eluates into two well-separated elution peaks, multi-angle light scattering analysis pointed out that the two peaks correspond to monomeric species with the same molecular mass, indicating that this NOA double mutant adopts two different monomeric forms in solution (Figure S5E, low panel). One monomeric species appears to be more elongated with a higher frictional coefficient compared with the second monomeric species, which displays the same elution profile as that observed with the WT and the L351/Q354A/Q355A triple mutant. Because the proline can adopt two *cis* and *trans* conformations in protein, the presence of this less compact second monomeric species is compatible with the F363P substitution in the NOA double mutant.

Moreover, the SDS-PAGE analysis under non-reducing conditions points out that the dimerization properties of the D363R/F363P double mutant are partially altered as compared with the WT, whereas those of the L351/Q354A/Q355A triple mutant are totally abolished (Figure S5D). Thus, the triple mutation induces a more destabilizing effect on CEP55 NOA dimerization than the double mutant. In the light of the structural model shown in Figure 5, it is tempting to speculate that each Q354 of one monomer makes a specific hydrogen bound with the sulfur atom of each M356 belonging to the second monomer, giving a possible explanation why a drastic destabilization of the CEP55 NOA dimeric state was observed with the L351A/Q354A/Q355A triple mutant. Notably, it is worth pointing out that a tight coupling between dimerization and ubiquitin binding was previously observed upon studies with the NOA/CC2-LZ domain of NEMO (Grubisha et al., 2010). Therefore, finding mutations in CEP55 NOA, which only alter ubiquitin binding without interfering with the dimerization process, could be a challenging task, which could be insurmountable at the current stage without prior knowledge of the crystal structures of the apoform and complexed form of CEP55 NOA with a ubiquitin chain.

When analyzing ubiquitin-binding properties of CEP55 UBZ, different binding affinities were observed when we determined dissociation constants in solution by fluorescence polarization and BLI experiments. Even if we did not strictly compare the same type of K63-linked chain in FP (K63-UB_2) and BLI experiments

(K63-Ub_{2-7}), these differences in binding affinity cannot probably be due to the differences of the chain length. First, the mixture of K63-linked UB_{2-7} chains used in BLI experiments mainly contains di-ubiquitin and tri-ubiquitin chains and only a minor amount of Ub_{4-7} chains. Second, the experimental conditions used in solution and BLI experiments were different. Indeed, the DDM detergent was added at 0.1% in FP experiments because it was required to prevent the non-specific binding between ubiquitin and the fluorescein conjugated to CEP55 UBZ. This may considerably reduce the ubiquitin-binding constant by disrupting the hydrophobic interactions on the I44-centered hydrophobic interface of ubiquitin. Moreover, the ubiquitin chain used was in solution in FP experiments, whereas it was immobilized in BLI experiments. This could affect the binding entropy and may contribute to the difference of binding affinity observed between solution and BLI binding studies. Similar conflicting results between solution and pull-down binding studies were also reported with TAB2 NZF to assess the linkage selectivity between K48 and K63 Ub_2 and Ub_4 chains (Kulathu et al., 2009).

Strikingly, we observed that the CEP55 ΔZF-UBZ^{RAD18} chimeric protein completely restored CEP55 midbody recruitment like the WT, whereas all the other chimeric proteins tested only partially compensate for the phenotype (Figure 7D). A possible explanation could be the binding mode of UBZ^{RAD18} and its ubiquitin-linkage preference for K63 and linear chains over K48 chains, which appeared to be more similar to those of UBZ^{CEP55}. However, one cannot rule out the possibility that this best compensation effect was also due to the additional ELRM motif located at the C terminus of UBZ^{RAD18} (Thach et al., 2015), which can confer a better binding affinity to polyubiquitin chains compared with all the other UBZs and nZFs tested.

Importantly, recent studies reported that CEP55 mutations are responsible for two human pathologies named MARCH (Frosk et al., 2017) and Meckel-like syndrome (Bondeson et al., 2017; Rawlins et al., 2019), which exhibit some similar clinical signs. Hypomorphic CEP55 mutations were found to be associated with MARCH, which is a severe and autosomal-recessive syndrome that affects neuronal mitosis. The developmental features of MARCH include hydranencephaly, anhydramnios, renal dysplasia, and cerebellar hypoplasia. Amorphic CEP55 mutations were reported to be associated with the Meckel-like syndrome and with *in utero* lethality. This syndrome is linked to cilia-related disorders, called ciliopathies, and some clinical signs detected in the affected fetus are similar with MARCH, including aberrant developments of brain and cerebellum, renal cysts, and oligohydramnios. Importantly, the MARCH-related p.S425X mutation (c.1274C > A), which has a similar CEP55 expression level as that of a healthy patient control (Frosk et al., 2017), corresponds to a deletion of the UBZ. Strikingly, this p.S425X mutation exhibits a defect in CEP55 recruitment to the midbody like the C440A/C443A debilitating double mutant investigated in the present study. Therefore, it is tempting to speculate that all mutations of CEP55 that alter the UBZ structure by modifying the zinc-ion-coordinating residues (C440, C443, H458, and C462) or that impair its ubiquitin-binding properties like the E460A single mutant may also lead to the MARCH syndrome. It is also tempting to predict that the extent and severity of the clinical signs found in MARCH and Meckel-like syndromes could be correlated with mutations found in the CEP55 NOA and UBZ domains, taking into account our findings that mutations located in CEP55 UBZ lead to a more severe defect in cytokinetic abscission than those contained in NOA.

Live-cell imaging with super resolution microscopy using live PALM experiments supports the view that NEMO induces dynamic condensates with liquid-like properties (Scholefield et al., 2016), which are reminiscent of the formation of membrane-less compartments induced by liquid phase separation (Banani et al., 2017). We previously showed that these NEMO condensates are mediated by the C-terminal bipartite UBD of NEMO and the multivalent interactions with M1- and K63-linked polyubiquitin chains. Like NEMO, and its Optineurin and ABIN2 related proteins, CEP55 likely forms an elongated coiled-coil structure with two similar folded UBDs in its C-terminal part that are interspersed by a disordered linker of 30–50 amino acids rich in hydrophobic Pro residues. Such a bipartite domain and CEP55 oligomerization could favor multivalent-multivalent interactions with extended conformations of M1- and K63-linked polyubiquitin chains, facilitating formation of membrane-less biomolecular condensate through liquid phase separation. These multivalent interactions could guide the assembly with midbody-associated proteins required for cytokinesis such as MKLP-1 and ALIX proteins. Consistent with this hypothesis, we observed impaired interactions of the C440A/C443A debilitating UBZ mutant of CEP55 with MKLP-1 and ALIX in preliminary experiments. Further characterization of CEP55 and its ubiquitin-mediated protein assembly should provide deeper insights into the mechanism by which CEP55 is tightly regulated in cytokinesis and may contribute to open therapeutic strategies for cancers.

Limitations of the Study

In this study, we have clearly shown that CEP55 contains two NEMO-like UBDs in its C-terminal part, which are both crucial for cytokinetic abscission in a ubiquitin-binding-dependent manner. However, neither the ubiquitinylated protein, which can be CEP55 itself, nor the ubiquitin ligase(s) that contribute to CEP55 recruitment to the midbody were identified in this study but are worth investigating in the future. Moreover, although structural models of CEP55 NOA and UBZ domains were validated by biophysical and biochemical data, determination of their true structures by NMR and/or crystallization, which proved more difficult than expected, is lacking and requires further investigation in the future.

METHODS

All methods can be found in the accompanying Transparent Methods supplemental file.

SUPPLEMENTAL INFORMATION

Supplemental Information can be found online at https://doi.org/10.1016/j.isci.2019.08.042.

ACKNOWLEDGMENTS

We thank N. Tarantino for technical assistance, A. Haouz (Crystallography Core Facility), P. England (Molecular Biophysics Core Facility), S. Petres (Production and Purification of Recombinant Proteins Core Facility), as well as M. Matondo, T. Chaze, and J. Chamot-Rooke (UtechS MSBio). We acknowledge A. Echard and M. Mhlanga for their advice and support. Funding was supplied by Ligue Nationale Contre le Cancer, Global Care Initiative, and Institut Carnot Pasteur MS (to F.A.); Ligue Nationale Contre le Cancer comité du Val-d'Oise and Fondation ARC pour la recherche sur le cancer (to E.L.).

AUTHOR CONTRIBUTIONS

Conceptualization, K.N.S.H., E.L., and F.A.; Methodology, K.N.S.H., E.F., A.B., M.C., L.D., M.B., E.L., and F.A.; Investigation, K.N.S.H., E.F., A.B., L.D., M.C., M.B., E.L., and F.A.; Formal Analysis, K.N.S.H., L.D., M.B., E.L., and F.A.; Resources, K.N.S.H., E.F., and M.C.; Project Administration, F.A.; Writing - Original Draft, K.N.S.H. and F.A.; Visualization, K.N.S.H., E.L., and F.A.; Writing - Review & Editing, K.N.S.H., R.W., A.I., E.L., and F.A.; Funding Acquisition and Supervision, E.L. and F.A.

DECLARATION OF INTERESTS

The authors declare no competing interests.

Received: March 27, 2019
Revised: July 15, 2019
Accepted: August 21, 2019
Published: October 25, 2019

REFERENCES

Banani, S.F., Lee, H.O., Hyman, A.A., and Rosen, M.K. (2017). Biomolecular condensates: organizers of cellular biochemistry. Nat. Rev. Mol. Cell Biol. *18*, 285–298.

Bastos, R.N., and Barr, F.A. (2010). Plk1 negatively regulates Cep55 recruitment to the midbody to ensure orderly abscission. J. Cell Biol. *191*, 751–760.

Bomar, M.G., Pai, M.T., Tzeng, S.R., Li, S.S., and Zhou, P. (2007). Structure of the ubiquitin-binding zinc finger domain of human DNA Y-polymerase eta. EMBO Rep. *8*, 247–251.

Bondeson, M.L., Ericson, K., Gudmundsson, S., Ameur, A., Ponten, F., Wesstrom, J., Frykholm, C., and Wilbe, M. (2017). A nonsense mutation in CEP55 defines a new locus for a Meckel-like syndrome, an autosomal recessive lethal fetal ciliopathy. Clin. Genet. *92*, 510–516.

Carlton, J.G., and Martin-Serrano, J. (2007). Parallels between cytokinesis and retroviral budding: a role for the ESCRT machinery. Science *316*, 1908–1912.

Carlton, J.G., Agromayor, M., and Martin-Serrano, J. (2008). Differential requirements for Alix and ESCRT-III in cytokinesis and HIV-1 release. Proc. Natl. Acad. Sci. U S A *105*, 10541–10546.

Chen, C.T., Ettinger, A.W., Huttner, W.B., and Doxsey, S.J. (2013). Resurrecting remnants: the lives of post-mitotic midbodies. Trends Cell Biol. *23*, 118–128.

Cordier, F., Grubisha, O., Traincard, F., Veron, M., Delepierre, M., and Agou, F. (2009). The zinc finger of NEMO is a functional ubiquitin-binding domain. J. Biol. Chem. *284*, 2902–2907.

Crowell, E.F., Gaffuri, A.L., Gayraud-Morel, B., Tajbakhsh, S., and Echard, A. (2014). Engulfment of the midbody remnant after cytokinesis in mammalian cells. J. Cell Sci. *127*, 3840–3851.

Emmerich, C.H., Ordureau, A., Strickson, S., Arthur, J.S., Pedrioli, P.G., Komander, D., and Cohen, P. (2013). Activation of the canonical IKK complex by K63/M1-linked hybrid ubiquitin chains. Proc. Natl. Acad. Sci. U S A *110*, 15247–15252.

Ettinger, A.W., Wilsch-Brauninger, M., Marzesco, A.M., Bickle, M., Lohmann, A., Maliga, Z., Karbanova, J., Corbeil, D., Hyman, A.A., and Huttner, W.B. (2011). Proliferating versus differentiating stem and cancer cells exhibit distinct midbody-release behaviour. Nat. Commun. *2*, 503.

Fabbro, M., Zhou, B.B., Takahashi, M., Sarcevic, B., Lal, P., Graham, M.E., Gabrielli, B.G., Robinson, P.J., Nigg, E.A., Ono, Y., and Khanna, K.K. (2005). Cdk1/Erk2- and Plk1-dependent phosphorylation of a centrosome protein, Cep55, is required for its recruitment to midbody and cytokinesis. Dev. Cell *9*, 477–488.

Frosk, P., Arts, H.H., Philippe, J., Gunn, C.S., Brown, E.L., Chodirker, B., Simard, L., Majewski, J., Fahiminiya, S., Russell, C., et al. (2017). A truncating mutation in CEP55 is the likely cause of MARCH, a novel syndrome affecting neuronal mitosis. J. Med. Genet. *54*, 490–501.

Ganem, N.J., Storchova, Z., and Pellman, D. (2007). Tetraploidy, aneuploidy and cancer. Curr. Opin. Genet. Dev. *17*, 157–162.

Gershony, O., Pe'er, T., Noach-Hirsh, M., Elia, N., and Tzur, A. (2014). Cytokinetic abscission is an acute G1 event. Cell Cycle *13*, 3436–3441.

Grubisha, O., Kaminska, M., Duquerroy, S., Fontan, E., Cordier, F., Haouz, A., Raynal, B., Chiaravalli, J., Delepierre, M., Israel, A., et al. (2010). DARPin-assisted crystallography of the CC2-LZ domain of NEMO reveals a coupling between dimerization and ubiquitin binding. J. Mol. Biol. *395*, 89–104.

Hu, Q., Botuyan, M.V., Cui, G., Zhao, D., and Mer, G. (2017). Mechanisms of ubiquitin-nucleosome recognition and regulation of 53bp1 chromatin recruitment by RNF168/169 and RAD18. Mol. Cell *66*, 473–487.e9.

Hubeau, M., Ngadjeua, F., Puel, A., Israel, L., Feinberg, J., Chrabieh, M., Belani, K., Bodemer, C., Fabre, I., Plebani, A., et al. (2011). New mechanism of X-linked anhidrotic ectodermal dysplasia with immunodeficiency: impairment of ubiquitin binding despite normal folding of NEMO protein. Blood *118*, 926–935.

Kamranvar, S.A., Gupta, D.K., Huang, Y., Gupta, R.K., and Johansson, S. (2016). Integrin signaling via FAK-Src controls cytokinetic abscission by decelerating PLK1 degradation and subsequent recruitment of CEP55 at the midbody. Oncotarget *7*, 30820–30830.

Komander, D., and Rape, M. (2012). The ubiquitin code. Annu. Rev. Biochem. *81*, 203–229.

Kulathu, Y., Akutsu, M., Bremm, A., Hofmann, K., and Komander, D. (2009). Two-sided ubiquitin binding explains specificity of the TAB2 NZF domain. Nat. Struct. Mol. Biol. *16*, 1328–1330.

Kuo, T.C., Chen, C.T., Baron, D., Onder, T.T., Loewer, S., Almeida, S., Weismann, C.M., Xu, P., Houghton, J.M., Gao, F.B., et al. (2011). Midbody accumulation through evasion of autophagy contributes to cellular reprogramming and tumorigenicity. Nat. Cell Biol. *13*, 1214–1223.

Laplantine, E., Fontan, E., Chiaravalli, J., Lopez, T., Lakisic, G., Veron, M., Agou, F., and Israel, A. (2009). NEMO specifically recognizes K63-linked poly-ubiquitin chains through a new bipartite ubiquitin-binding domain. EMBO J. *28*, 2885–2895.

Lee, H.H., Elia, N., Ghirlando, R., Lippincott-Schwartz, J., and Hurley, J.H. (2008). Midbody targeting of the ESCRT machinery by a noncanonical coiled coil in CEP55. Science *322*, 576–580.

Lin, S.M., Lin, S.C., Hong, J.Y., Su, T.W., Kuo, B.J., Chang, W.H., Tu, Y.F., and Lo, Y.C. (2017). Structural insights into linear tri-ubiquitin recognition by A20-binding inhibitor of NF-kappaB, ABIN-2. Structure *25*, 66–78.

Matsumoto, M.L., Wickliffe, K.E., Dong, K.C., Yu, C., Bosanac, I., Bustos, D., Phu, L., Kirkpatrick, D.S., Hymowitz, S.G., et al. (2010). K11-linked polyubiquitination in cell cycle control revealed by a K11 linkage-specific antibody. Mol. Cell *39*, 477–484.

Mierzwa, B., and Gerlich, D.W. (2014). Cytokinetic abscission: molecular mechanisms and temporal control. Dev. Cell *31*, 525–538.

Morita, E., Sandrin, V., Chung, H.Y., Morham, S.G., Gygi, S.P., Rodesch, C.K., and Sundquist, W.I. (2007). Human ESCRT and ALIX proteins interact with proteins of the midbody and function in cytokinesis. EMBO J. *26*, 4215–4227.

Mukai, A., Mizuno, E., Kobayashi, K., Matsumoto, M., Nakayama, K.I., Kitamura, N., and Komada, M. (2008). Dynamic regulation of ubiquitylation and deubiquitylation at the central spindle during cytokinesis. J. Cell Sci. *121*, 1325–1333.

Nakazawa, S., Oikawa, D., Ishii, R., Ayaki, T., Takahashi, H., Takeda, H., Ishitani, R., Kamei, K., Takeyoshi, I., Kawakami, H., et al. (2016). Linear ubiquitination is involved in the pathogenesis of optineurin-associated amyotrophic lateral sclerosis. Nat. Commun. *7*, 12547.

Ngadjeua, F., Chiaravalli, J., Traincard, F., Raynal, B., Fontan, E., and Agou, F. (2013). Two-sided ubiquitin binding of NF-kappaB essential modulator (NEMO) zinc finger unveiled by a mutation associated with anhidrotic ectodermal dysplasia with immunodeficiency syndrome. J. Biol. Chem. *288*, 33722–33737.

Pohl, C., and Jentsch, S. (2008). Final stages of cytokinesis and midbody ring formation are controlled by BRUCE. Cell *132*, 832–845.

Rahighi, S., Ikeda, F., Kawasaki, M., Akutsu, M., Suzuki, N., Kato, R., Kensche, T., Uejima, T., Bloor, S., Komander, D., et al. (2009). Specific recognition of linear ubiquitin chains by NEMO is important for NF-kappaB activation. Cell *136*, 1098–1109.

Rawlins, L.E., Jones, H., Wenger, O., Aye, M., Fasham, J., Harlalka, G.V., Chioza, B.A., Miron, A., Ellard, S., Wakeling, M., et al. (2019). An Amish founder variant consolidates disruption of CEP55 as a cause of hydranencephaly and renal dysplasia. Eur. J. Hum. Genet. *27*, 657–662.

Scholefield, J., Henriques, R., Savulescu, A.F., Fontan, E., Boucharlat, A., Laplantine, E., Smahi, A., Israel, A., Agou, F., and Mhlanga, M.M. (2016). Super-resolution microscopy reveals a preformed NEMO lattice structure that is collapsed in incontinentia pigmenti. Nat. Commun. *7*, 12629.

St-Denis, N., Gupta, G.D., Lin, Z.Y., Gonzalez-Badillo, B., Pelletier, L., and Gingras, A.C. (2015). Myotubularin-related proteins 3 and 4 interact with polo-like kinase 1 and centrosomal protein of 55 kDa to ensure proper abscission. Mol. Cell Proteomics *14*, 946–960.

Suzuki, N., Rohaim, A., Kato, R., Dikic, I., Wakatsuki, S., and Kawasaki, M. (2016). A novel mode of ubiquitin recognition by the ubiquitin-binding zinc finger domain of WRNIP1. FEBS J. *283*, 2004–2017.

Thach, T.T., Lee, N., Shin, D., Han, S., Kim, G., Kim, H., and Lee, S. (2015). Molecular determinants of polyubiquitin recognition by continuous ubiquitin-binding domains of Rad18. Biochemistry *54*, 2136–2148.

Toma, A., Takahashi, T.S., Sato, Y., Yamagata, A., Goto-Ito, S., Nakada, S., Fukuto, A., Horikoshi, Y., Tashiro, S., and Fukai, S. (2015). Structural basis for ubiquitin recognition by ubiquitin-binding zinc finger of FAAP20. PLoS One *10*, e0120887.

Wagner, S., Carpentier, I., Rogov, V., Kreike, M., Ikeda, F., Lohr, F., Wu, C.J., Ashwell, J.D., Dotsch, V., Dikic, I., and Beyaert, R. (2008). Ubiquitin binding mediates the NF-kappaB inhibitory potential of ABIN proteins. Oncogene *27*, 3739–3745.

Xie, X., Li, F., Wang, Y., Wang, Y., Lin, Z., Cheng, X., Liu, J., Chen, C., and Pan, L. (2015). Molecular basis of ubiquitin recognition by the autophagy receptor CALCOCO2. Autophagy *11*, 1775–1789.

Zhao, W.M., Seki, A., and Fang, G. (2006). Cep55, a microtubule-bundling protein, associates with centralspindlin to control the midbody integrity and cell abscission during cytokinesis. Mol. Biol. Cell *17*, 3881–3896.

ISCI, Volume *20*

Supplemental Information

Two NEMO-like Ubiquitin-Binding Domains in CEP55 Differently Regulate Cytokinesis

Keïs Nabhane Said Halidi, Elisabeth Fontan, Alix Boucharlat, Laurianne Davignon, Marine Charpentier, Mikaël Boullé, Robert Weil, Alain Israël, Emmanuel Laplantine, and Fabrice Agou

Supplemental Figure Legends and Figures

FIGURE S1

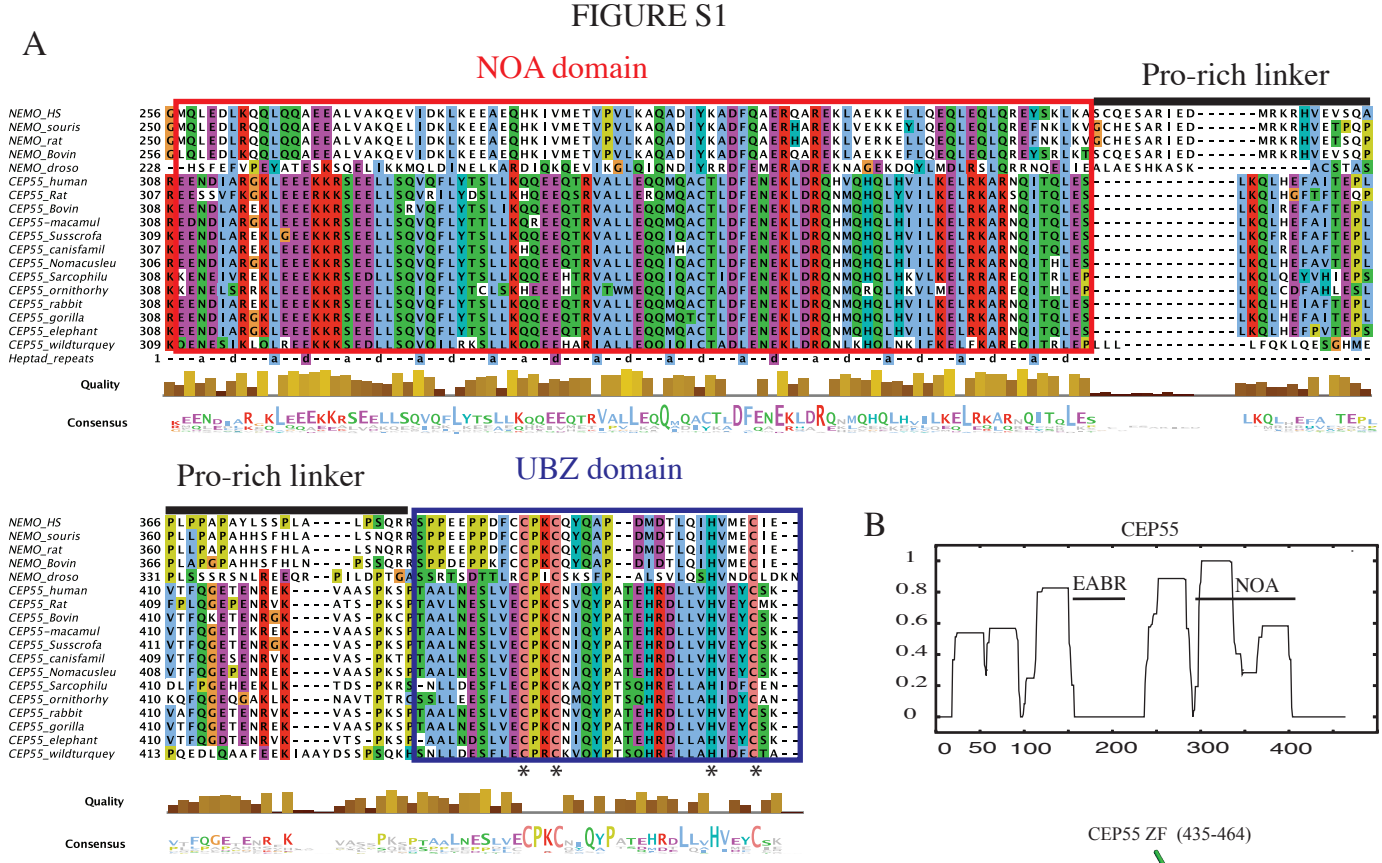

Figure S1. CEP55 contains two NOA and UBZ ubiquitin binding domains (UBDs) in its C-terminal part, which are similar to those of the NEMO protein, Related to Figure 1

(A) Multiple sequence alignment of CEP55 and NEMO from different organisms showing the degree of conservation of NOA (also called UBAN/CC2-LZ/CoZi/NUB) and UBZ UBD domains in each protein. Sequences were aligned with CLUSTAL Omega using software Jalview 2.10.1. The NOA and UBZ UBDs are boxed in red and blue, respectively. The conserved residues are highlighted by the default color scheme in Clustal X and zinc-ion-coordinating residues are indicated by an asterisk at the bottom of the sequence. (B) Schematic representation of the coiled-coil prediction of human CEP55 by Paircoil 2 program. The region corresponding to the NOA and EABR (ESCRT and ALIX binding region) domains are indicated. (C) Structural model of the dimeric coiled-coil NOA of CEP55 generated by homology modeling using the human NEMO NOA domain as template (PDB ID: 4BWN). (D) Structural model of CEP55 ZF generated by homology modeling using NEMO ZF as template (PDB ID: 2JVX). The Zn^{2+} ion is depicted as a grey sphere. (E) Structural model of CEP55 NOA model (green) showing that the Cys359 residues (orange) of each monomer are in close proximity when the domain forms a dimeric coiled-coil structure. The Cys359 residue depicted as a stick model corresponds to [d] position in the seven-residue heptad repeat of parallel dimeric coiled-coil and so contributes to the dimeric core and packing of two α-helices in the dimer. (F) SDS-PAGE analysis of purified CEP55 His-NOA under reducing or non-reducing conditions showing that each Cys359 is able to form a reversible disulfide bound between each monomer in the dimer. (G) Quantitative ubiquitin binding of CEP55 ZF with mono-ubiquitin or (H) a K63 di-ubiquitin chain in solution monitored by fluorescence polarization. Fluorescein labeled ZF noted F-ZF^{CEP55} (0.5 μM) was titrated with increasing concentrations of mono-ubiquitin (0-1000 μM) or K63 di-ubiquitin (0-500) μM.

FIGURE S2

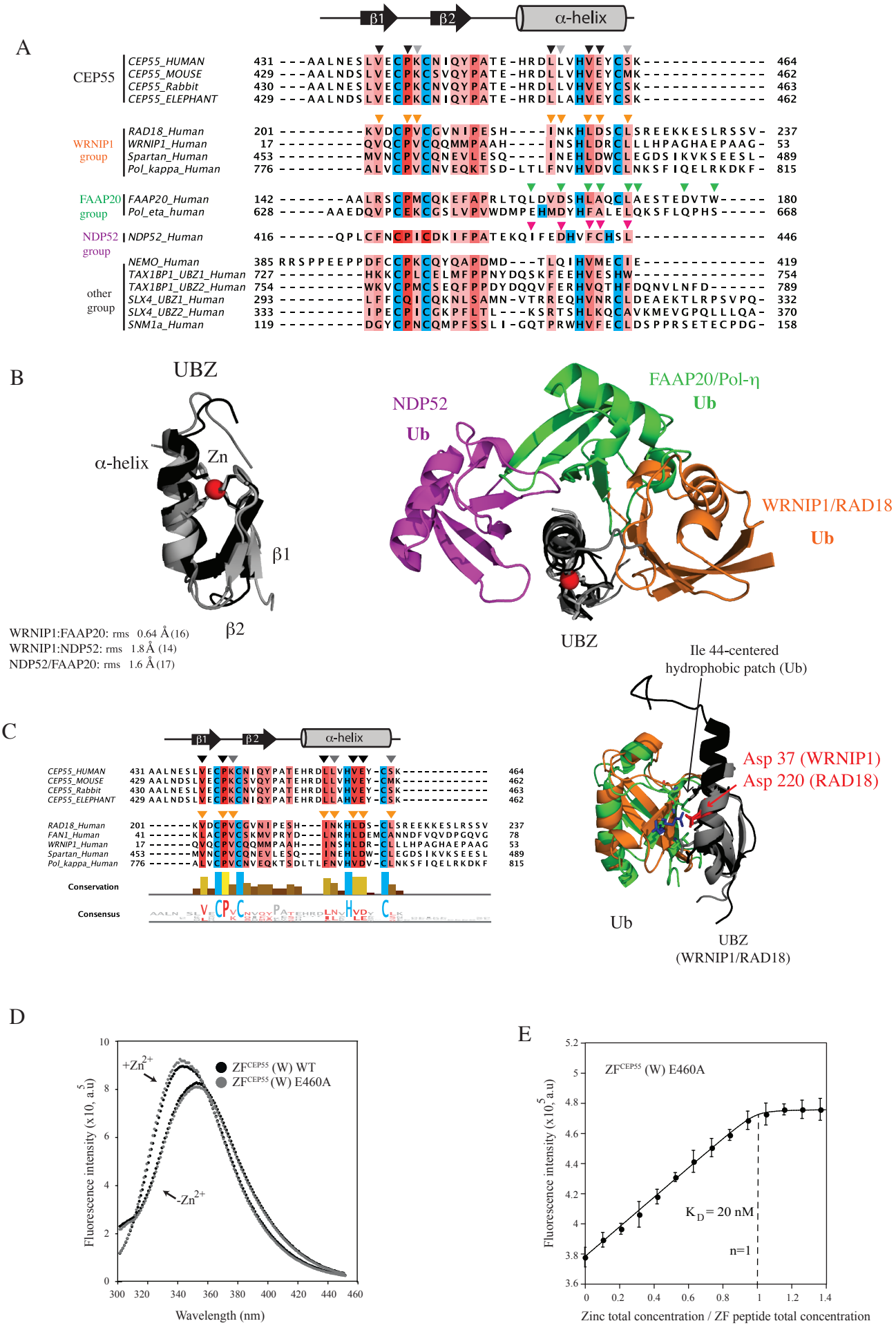
A
β1
β2
α-helix
CEP55
CEP55_HUMAN 431 ---AALNESLVECPKCNIQYPATE-HRDLLVHVEYCSK---------- 464
CEP55_MOUSE 429 ---AALNDSLVECPKCSVQYPATE-HRDLLVHVEYCMK---------- 462
CEP55_Rabbit 430 ---AALNESLVECPKCNVQYPATE-HRDLLVHVEYCSK---------- 463
CEP55_ELEPHANT 429 ---AALNDSLVECPKCNIQYPATE-HRDLLAHVEYCSK---------- 462
WRNIP1 group
RAD18_Human 201 ---------KVDCPVCGVNIPESH----INKHLDSCLSREEKKESLRSSV- 237
WRNIP1_Human 17 ---------QVQCPVCQQMMPAAH----INSHLDRCLLLHPAGHAEPAAG- 53
Spartan_Human 453 ---------MVNCPVCQNEVLESQ----INEHLDWCLEGDSIKVKSEESL- 489
Pol_kappa_Human 776 ---------ALVCPVCNVEQKTSD-LTLFNVHVDVCLNKSFIQELRKDKF- 815
FAAP20 group
FAAP20_Human 142 -------AALRSCPMCQKEFAPRLTQLDVDSHLAQCLAESTEDVTW----- 180
Pol_eta_human 628 -----AAEDQVPCEKCGSLVPVWDMPEHMDYHFALELQKSFLQPHS----- 668
NDP52 group
NDP52_Human 416 ------QPLCFNCPICDKIFPATEKQIFEDHVFCHSL---------- 446
other group
NEMO_Human 385 RRSPPEEPPDFCCPKCQYQAPDMD---TLQIHVMECIE---------- 419
TAX1BP1_UBZ1_Human 727 ---------HKKCPLCELMFPPNYDQSKFEEHVESHW---------- 754
TAX1BP1_UBZ2_Human 754 ---------WKVCPMCSEQFPPDYDQQVFERHVQTHFDQNVLNFD------ 789
SLX4_UBZ1_Human 293 ---------LFFCQICQKNLSAMN-VTRREQHVNRCLDEAEKTLRPSVPQ- 332
SLX4_UBZ2_Human 333 ---------IPECPICGKPFLTL---KSRTSHLKQCAVKMEVGPQLLLQA- 370
SNM1a_Human 119 ---------DGYCPNCQMPFSSLI-GQTPRWHVFECLDSPPRSETECPDG- 158
B
UBZ
α-helix
Zn
β1
β2
WRNIP1:FAAP20: rms 0.64 Å (16)
WRNIP1:NDP52: rms 1.8 Å (14)
NDP52/FAAP20: rms 1.6 Å (17)
NDP52
Ub
FAAP20/Pol-η
Ub
WRNIP1/RAD18
Ub
UBZ
C
β1
β2
α-helix
CEP55_HUMAN 431 AALNESLVECPKCNIQYPATEHRDLLVHVEY-CSK---------- 464
CEP55_MOUSE 429 AALNDSLVECPKCSVQYPATEHRDLLVHVEY-CMK---------- 462
CEP55_Rabbit 430 AALNESLVECPKCNVQYPATEHRDLLVHVEY-CSK---------- 463
CEP55_ELEPHANT 429 AALNDSLVECPKCNIQYPATEHRDLLAHVEY-CSK---------- 462
RAD18_Human 201 ------KVDCPVCGVNIPESH---INKHLDS-CLSREEKKESLRSSV 237
FAN1_Human 41 ------KLACPVCSKMVPRYD---LNRHLDEMCANNDFVQVDPGQVG 78
WRNIP1_Human 17 ------QVQCPVCQQMMPAAH---INSHLDR-CLLLHPAGHAEPAAG 53
Spartan_Human 453 ------MVNCPVCQNEVLESQ---INEHLDW-CLEGDSIKVKSEESL 489
Pol_kappa_Human 776 ------ALVCPVCNVEQKTSDLTLFNVHVDV-CLNKSFIQELRKDKF 815
Conservation
Consensus
Ile 44-centered
hydrophobic patch (Ub)
Asp 37 (WRNIP1)
Asp 220 (RAD18)
Ub
UBZ
(WRNIP1/RAD18)
D
+Zn2+
-Zn2+
ZFCEP55 (W) WT
ZFCEP55 (W) E460A
Fluorescence intensity (x10, a.u)
Wavelength (nm)
E
ZFCEP55 (W) E460A
KD = 20 nM
n=1
Fluorescence intensity (x10, a.u)
Zinc total concentration / ZF peptide total concentration

Figure S2. The CEP55 ZF displays the highest homology with the RAD18/WRINP1 UBZ group, suggesting a similar ubiquitin binding mode, Related to Figure 3

(A) Structure-based sequence alignment of CEP55 ZF with different UBZs classified into at least 4 different UBZ groups according to their mode of ubiquitin recognition. The sequences of human NDP52 (also called CALCOCO2) and human Polη were aligned, based on their 3D structures. Zinc-ion-coordinating residues are highlighted in blue, whereas those that interact with ubiquitin in the complex structure of WRNIP1/RAD18, FAAP20/polη and NDP52 are indicated by yellow, green and magenta inverted triangles on the top of each sequence, respectively. The secondary structure elements of CEP55 ZF are illustrated as a tube for the α-helix and arrows for β strands above the sequence. Black and grey inverted triangles indicate highly and partially conserved residues, which make interactions with ubiquitin. (B) Comparison of crystal complexes of different UBZ groups with ubiquitin. Superposition of UBZ structures of WRNP1 (PDB ID: 3VHT), FAAP20 (PDB ID: 3WWQ) and NDP52 (PDB ID: 4XKL) alone (left) or in complex with ubiquitin (right). In each UBZ, the Zn^{2+} ion is depicted as a red sphere. For clarity, only the distal ubiquitin of K63-Ub_2 is shown with the complex FAAP20:K63-Ub_2. Color scheme is the same as in (A). (C) Left, sequence alignment of CEP55 ZF from different organisms with human members of the WRNIP1/RAD18 group. Sequences were aligned using CLUSTAL Ω. The highly and partially conserved residues are indicated by heavy and light red-shaded boxes, respectively. Right, comparison of crystal and NMR solution structures of WRNP1 (PDB ID: 3VHT, in grey) and RAD18 (PDB ID: 5VF0, in black) in complex with mono-ubiquitin (orange for WRNP1 and green RAD18). The strictly conserved Asp/Glu residue making a significant binding hot spot with ubiquitin (Arg 42) and located in the C-terminal of α-helix is shown as a stick model in red. (D) Fluorescence emission spectra of WT (black) and E460A mutant (grey) ZF^{CEP55} (W) peptides (10 μM) in presence or in absence of zinc ion at an excitation wavelength of 280 nm. (E) Titration of the E460A F-ZF^{CEP55} (W) mutant peptide (0.9 μM) using increasing zinc concentrations (0.1-1.2 μM) at an excitation and emission wavelengths of 280 and 347 nm, respectively. Error bars represent the standard deviation of the fluorescence measurements of each titration point for 5 min.

FIGURE S3

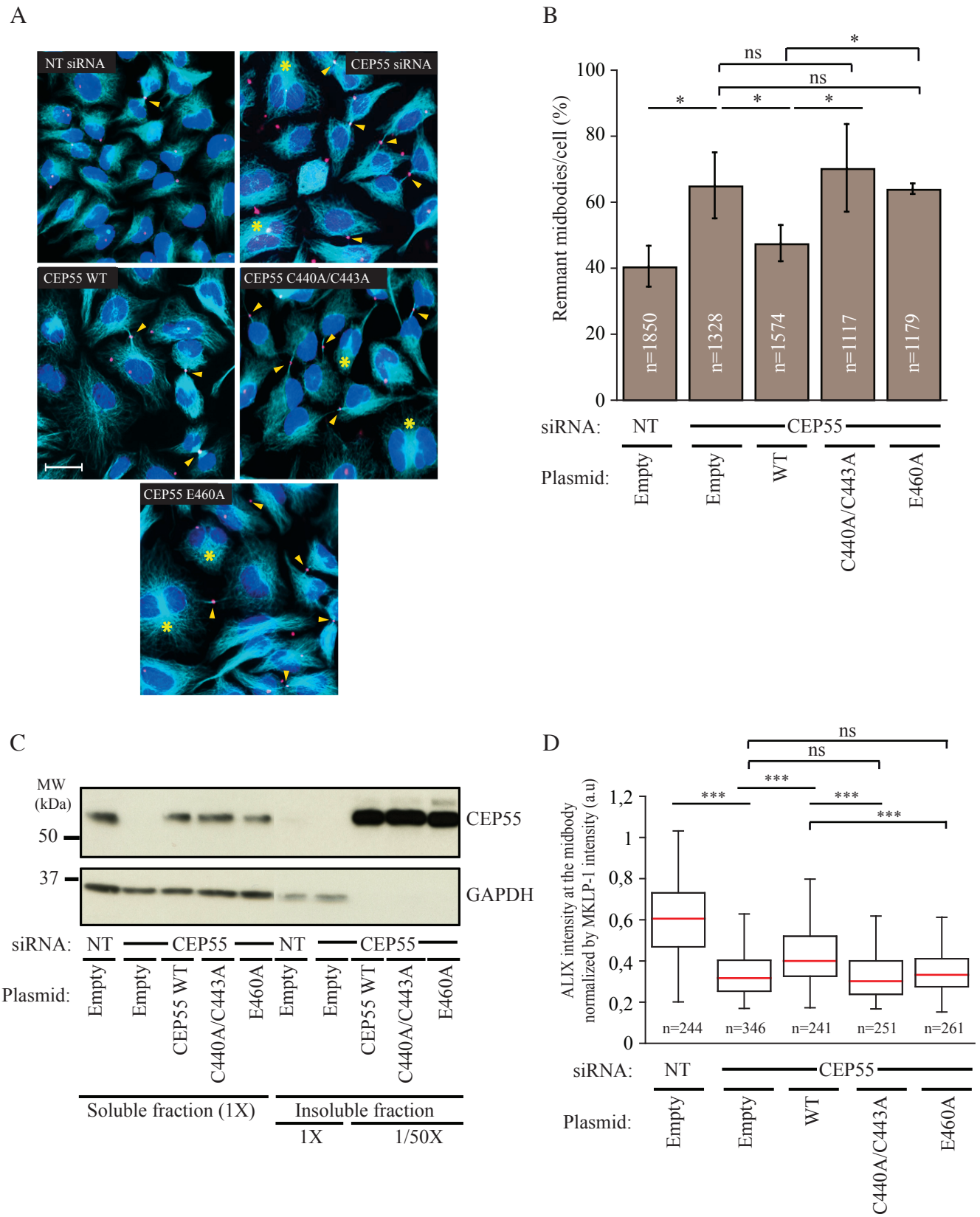
A
NT siRNA
CEP55 siRNA
CEP55 WT
CEP55 C440A/C443A
CEP55 E460A
B
Remnant midbodies/cell (%)
100
80
60
40
20
0
ns
ns
*
*
*
*
n=1850
n=1328
n=1574
n=1117
n=1179
siRNA: NT CEP55
Plasmid: Empty Empty WT C440A/C443A E460A
C
MW (kDa)
50
37
CEP55
GAPDH
siRNA: NT CEP55 NT CEP55
Plasmid: Empty Empty CEP55 WT C440A/C443A E460A Empty Empty CEP55 WT C440A/C443A E460A
Soluble fraction (1X)
Insoluble fraction
1X
1/50X
D
ALIX intensity at the midbody normalized by MKLP-1 intensity (a.u)
1,2
1
0,8
0,6
0,4
0,2
0
ns
ns
***
***
***
***
n=244
n=346
n=241
n=251
n=261
siRNA: NT CEP55
Plasmid: Empty Empty WT C440A/C443A E460A

Figure S3. CEP55 ZF is essential for recruitment to the midbody and proper abscission, Related to Figure 4

HeLa cells were concomitantly transfected with a non-targeting (NT) or CEP55 siRNA and with an empty vector or a CEP55 siRNA resistant vector encoding either HA-CEP55 WT, HA CEP55 C440A/C443A or HA-CEP55 E460A. (A) Cells were then stained with DAPI (blue), MKLP-1 (red) and β-tubulin (cyan) antibodies. Arrows and stars represent cells connected by a midbody and multinucleated cells, respectively. Image quantification is depicted in Figure 4 (A-B). Scale bar= 10 μM.

(B) Analysis of the ZF mutant ability to rescue the defect in midbody remnant clearance induced by CEP55 depletion. The images shown in (A) were used to quantify the ratio of midbody remnant per cell (%) as described in Transparent Methods. Data represent the mean ± SD of three independent experiments and the total number of nuclei (n) counted in the 3 experiments is indicated.

(C) The level of expression of CEP55 in the insoluble fraction of the western blot shown in Figure 4 was also controlled showing a similar level of expression between the different ectopic proteins, which are mainly expressed in the insoluble fraction.

(D) Quantification of ALIX intensity at the midbody under different experimental conditions. Cells were stained with DAPI, ALIX, MKLP-1 and β-tubulin antibodies. ALIX intensity was normalized by MKLP-1 intensity at the midbody upon MKLP-1 dots. The total numbers of midbodies (n) detected are indicated.

***$p < 0.001$; *$p < 0.05$; ns: not significant ($p \geq 0.05$).

FIGURE S4

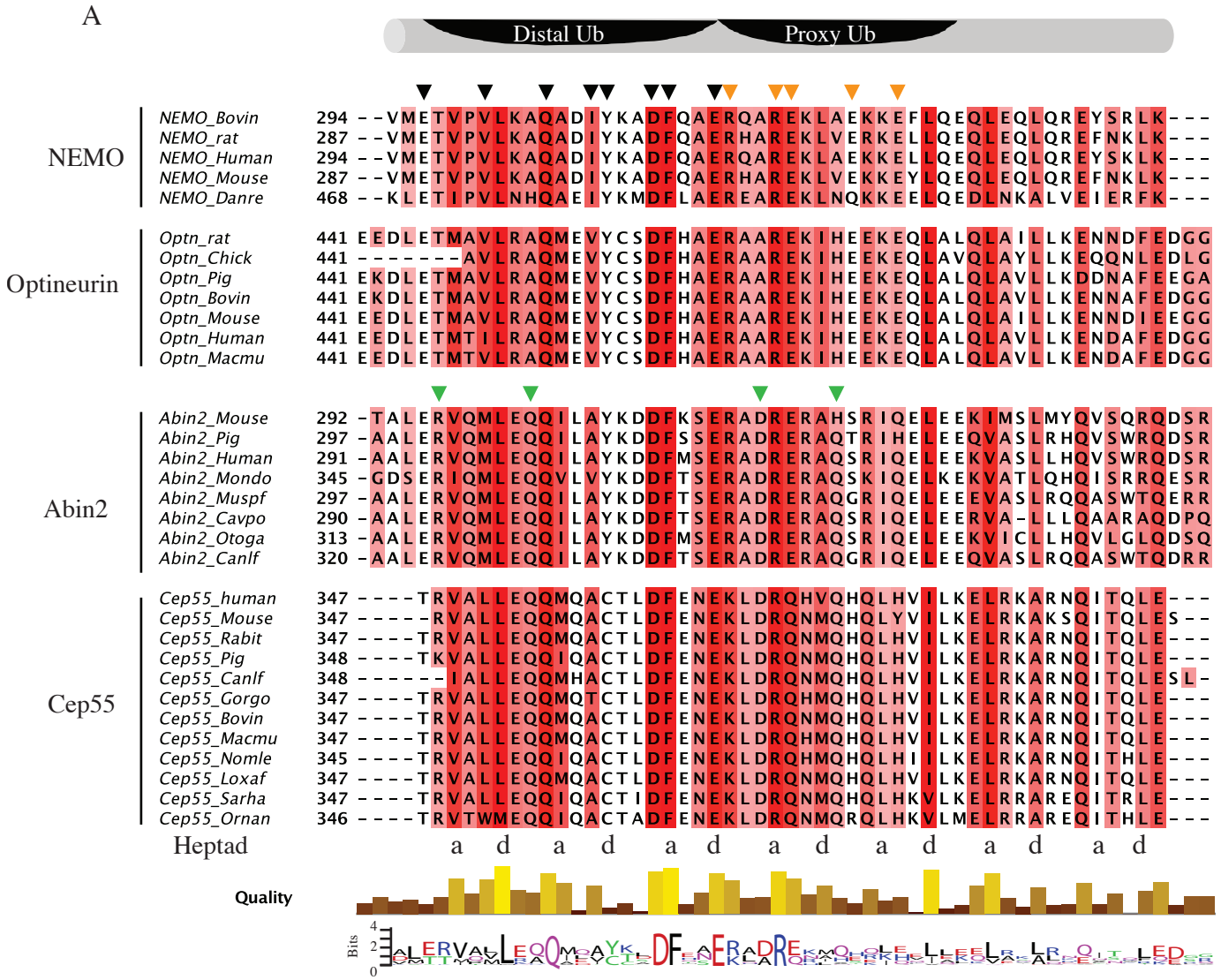
A
Distal Ub
Proxy Ub
NEMO
NEMO_Bovin 294 --VMETVPVLKAQADIYKADFQAERQAREKLAEKKEFLQEQLEQLQREYSRLK---
NEMO_rat 287 --VMETVPVLKAQADIYKADFQAERHAREKLVERKELLQEQLEQLQREFNKLK---
NEMO_Human 294 --VMETVPVLKAQADIYKADFQAERQAREKLAEKKELLQEQLEQLQREYSKLK---
NEMO_Mouse 287 --VMETVPVLKAQADIYKADFQAERHAREKLVEKKEYLQEQLEQLQREFNKLK---
NEMO_Danre 468 --KLETIPVLNHQAEIYKMDFLAERFAREKLNQKKEELQEDLNKALVEIERFK---
Optineurin
Optn_rat 441 EEDLETMAVLRAQMEVYCSDFHAERAAREKIHEEKEQLALQLAILLKENNDFEDGG
Optn_Chick 441 -------AVLRAQMEVYCSDFHAERAAREKIHEEKEQLAVQLAYLLKEQQNLEDLG
Optn_Pig 441 EKDLETMAVLRAQMEVYCSDFHAERAAREKIHEEKEQLALQLAVLLKDDNAFEEGA
Optn_Bovin 441 EKDLETMAVLRAQMEVYCSDFHAERAAREKIHEEKEQLALQLAVLLKENNAFEDGG
Optn_Mouse 441 EEDLETMAVLRAQMEVYCSDFHAERAAREKIHEEKEQLALQLAILLKENNDIEEGG
Optn_Human 441 EEDLETMTILRAQMEVYCSDFHAERAAREKIHEEKEQLALQLAVLLKENDAFEDGG
Optn_Macmu 441 EEDLETMTVLRAQMEVYCSDFHAERAAREKIHEEKEQLALQLAVLLKENDAFEDGG
Abin2
Abin2_Mouse 292 -TALERVQMLEQQILAYKDDFKSERADRERAHSRIQELEEKIMSLMYQVSQRQDSR
Abin2_Pig 297 -AALERVQMLEQQILAYKDDFSSERADRERAQTRIHELEEQVASLRHQVSWRQDSR
Abin2_Human 291 -AALERVQMLEQQILAYKDDFMSERADRERAQSRIQELEEKVASLLHQVSWRQDSR
Abin2_Mondo 345 -GDSERIQMLEQQVLVYKDDFTSERADRERAQSKIQELKEKVATLQHQISRRQESR
Abin2_Muspf 297 -AALERVQMLEQQILAYKDDFTSERADRERAQGRIQELEEEVASLRQQASWTQERR
Abin2_Cavpo 290 -AALERVQMLEQQILAYKDDFTSERADRERAQSRIQELEERVA-LLLQAARAQDPQ
Abin2_Otoga 313 -AALERVQMLEQQILAYKDDFMSERADRERAQSRIQELEEKVICLLHQVLGLQDSQ
Abin2_Canlf 320 -AALERVQMLEQQILAYKDDFTSERADRERAQGRIQELEEQVASLRQQASWTQDRR
Cep55
Cep55_human 347 ----TRVALLEQQMQACTLDFENEKLDRQHVQHQLHVILKELRKARNQITQLE---
Cep55_Mouse 347 -----RVALLEQQMQACTLDFENEKLDRQNMQHQLYVILKELRKAKSQITQLES--
Cep55_Rabit 347 ----TRVALLEQQMQACTLDFENEKLDRQNMQHQLHVILKELRKARNQITQLE---
Cep55_Pig 348 ----TKVALLEQQIQACTLDFENEKLDRQNMQHQLHVILKELRKARNQITQLE---
Cep55_Canlf 348 -------IALLEQQMHACTLDFENEKLDRQNMQHQLHVILKELRKARNQITQLESL-
Cep55_Gorgo 347 ----TRVALLEQQMQTCTLDFENEKLDRQHMQHQLHVILKELRKARNQITQLE---
Cep55_Bovin 347 ----TRVALLEQQMQACTLDFENEKLDRQNMQHQLHVILKELRKARNQITQLE---
Cep55_Macmu 347 ----TRVALLEQQMQACTLDFENEKLDRQHMQHQLHVILKELRKARNQITQLE---
Cep55_Nomle 345 ----TRVALLEQQIQACTLDFENEKLDRQHMQHQLHIILKELRKARNQITHLE---
Cep55_Loxaf 347 ----TRVALLEQQMQACTLDFENEKLDRQNMQHQLHVILKELRKARNQITQLE---
Cep55_Sarha 347 ----TRVALLEQQIQACTIDFENEKLDRQNMQHQLHKVLKELRRAREQITRLE---
Cep55_Ornan 346 ----TRVTWMEQQIQACTADFENEKLDRQNMQRQLHKVLMELRRARFQITHLE---
Heptad a d a d a d a d a d a d a d
Quality
Bits
B
NEMO
Optineurin (rms, 0.9 Å (146))
Abin2 (rms, 1.3 Å (146))
Distal Ub
Proxy Ub
NOA domain

Figure S4. Comparison of CEP55 NOA UBD with those of NEMO, Optineurin and ABIN2, Related to Figure 5

(A) Structure-based alignment of CEP55 NOA with NEMO, OPTINEURIN and ABIN2 from different species. Sequences were aligned with CLUSTAL Ω using software Jalview 2.10.1. The completely and partially conserved residues are highlighted by heavy and light red shaded boxes, respectively. The residues which are important for the NOA domain and distal ubiquitin of M1-Ub_2 (Distal Ub) are indicated by black inverted triangles, whereas those that make specific contacts with the proximal ubiquitin (Proxy Ub) by orange inverted triangles. The residues that are only conserved in ABIN2 and CEP55 families and that are important for both proximal and distal ubiquitin binding are indicated by green inverted triangles above the ABIN2 sequences. Letters immediately below the alignment indicate conserved residues in the a and d positions involved in the hydrophobic core of parallel coiled coil dimer structures of NEMO, OPTINEURIN and ABIN2. In this alignment, note that the residues previously shown as specifically involved in the linear linkage of M1-Ub_2 and proximal ubiquitin binding are not strictly conserved in CEP55 family. Indeed, the five Ub-interacting residues of NEMO NOA (*i.e.* Arg316, Arg319, Glu320, Glu324 and Glu327) are not conserved or replaced by a functionally equivalent residue in CEP55 NOA (*i.e.*, Lys367, Arg370, Gln371, His372 and His375). (B) The NOA UBD of NEMO, Optineurin and ABIN2 exhibit a conserved mode of recognition to a linear di-ubiquitin chain**.** Structural comparison of crystal complexes of different NOA domains in complex with a linear Ub_2 chain, showing a conserved linear di-ubiquitin binding mode. Root mean square (rms) differences between the superimposed NOA domain of NEMO in grey (PDB ID 2ZVO), OPTINEURIN in orange (PDB ID: 5B83) and ABIN2 in magenta (PDB ID 5H07) are indicated. The number of aligned atoms is indicated in parentheses.

FIGURE S5

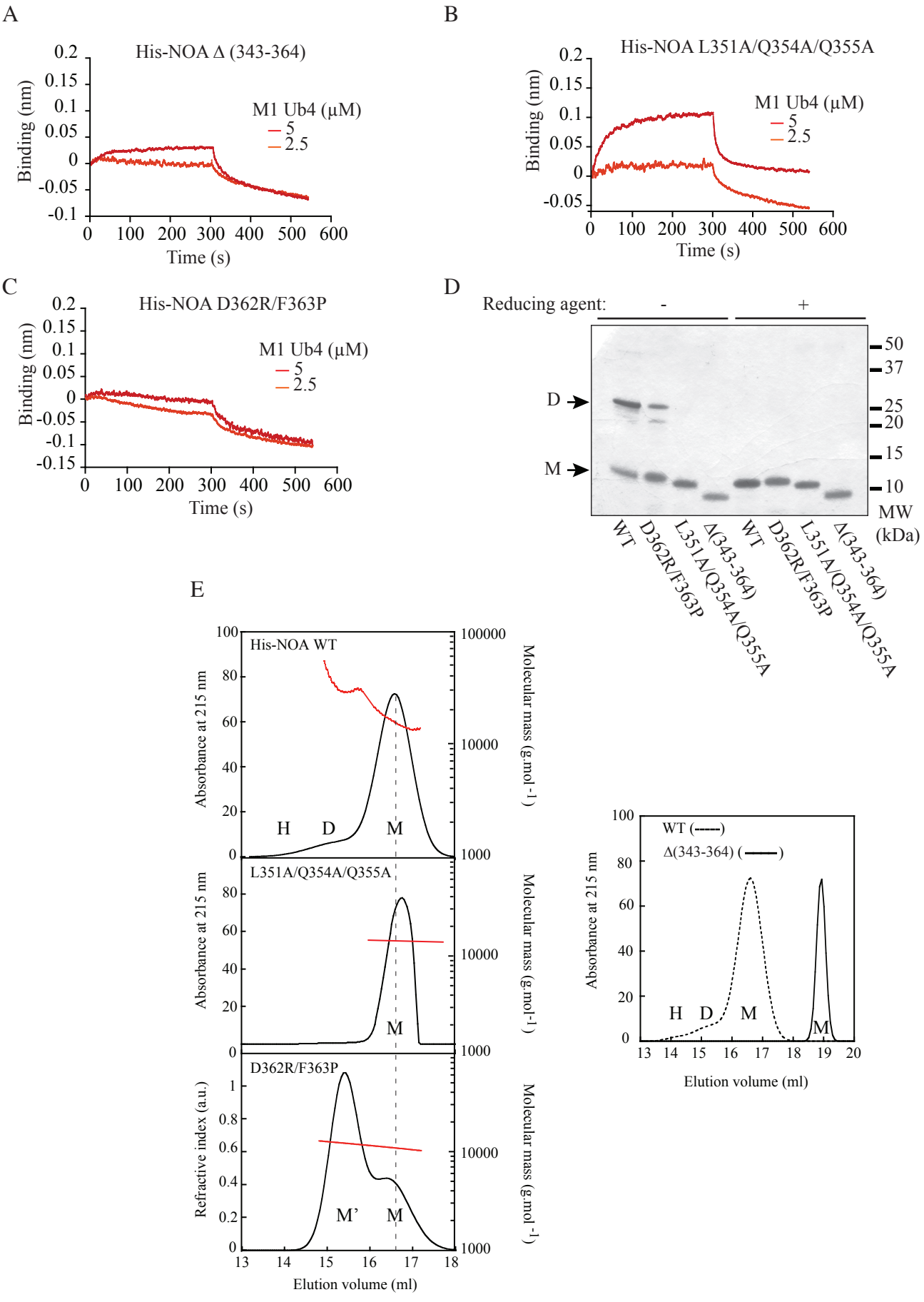
A
His-NOA Δ (343-364)
Binding (nm)
M1 Ub4 (μM)
5
2.5
Time (s)
B
His-NOA L351A/Q354A/Q355A
C
His-NOA D362R/F363P
D
Reducing agent:
D
M
MW (kDa)
WT
D362R/F363P
L351A/Q354A/Q355A
Δ(343-364)
E
His-NOA WT
L351A/Q354A/Q355A
D362R/F363P
Absorbance at 215 nm
Refractive index (a.u.)
Molecular mass (g mol-1)
H
D
M
M'
Elution volume (ml)
WT (------)
Δ(343-364) (——)

Figure S5. Ubiquitin binding affinity and dimer stability of CEP55 His-NOA and its three mutants, Related to Figure 5

Quantification of ubiquitin binding activity by biolayer interferometry (BLI) of His-NOA Δ(343-364) (A), His-NOA L531A/Q354A/Q355A (B) and His-NOA D362R/F363P mutants (C) with a linear tetra-ubiquitin chain (2.5-5 μM). His-NOA mutants (8 μM) were immobilized on anti-penta-his biosensors in all experiments.

(D) SDS-PAGE analyses of purified CEP55 His-NOA WT and its mutants under reducing or non-reducing conditions. Note that the His-NOA Δ(343-364) mutant, which has an internal deletion from residues 343-364, lacks the Cys359 residue and was then used as a negative control.

(E) Analysis of CEP55 His-NOA WT and its mutants by size exclusion chromatography coupled with multiangle light scattering (SEC-MALS). None of the mutants is able to dimerize and oligomerize under these experimental conditions (reducing conditions). M: first monomer species, M': second monomer species with a higher frictional coefficient compared to M (same molecular mass but different hydrodynamic properties), D: dimer, H: hexamer.

FIGURE S6

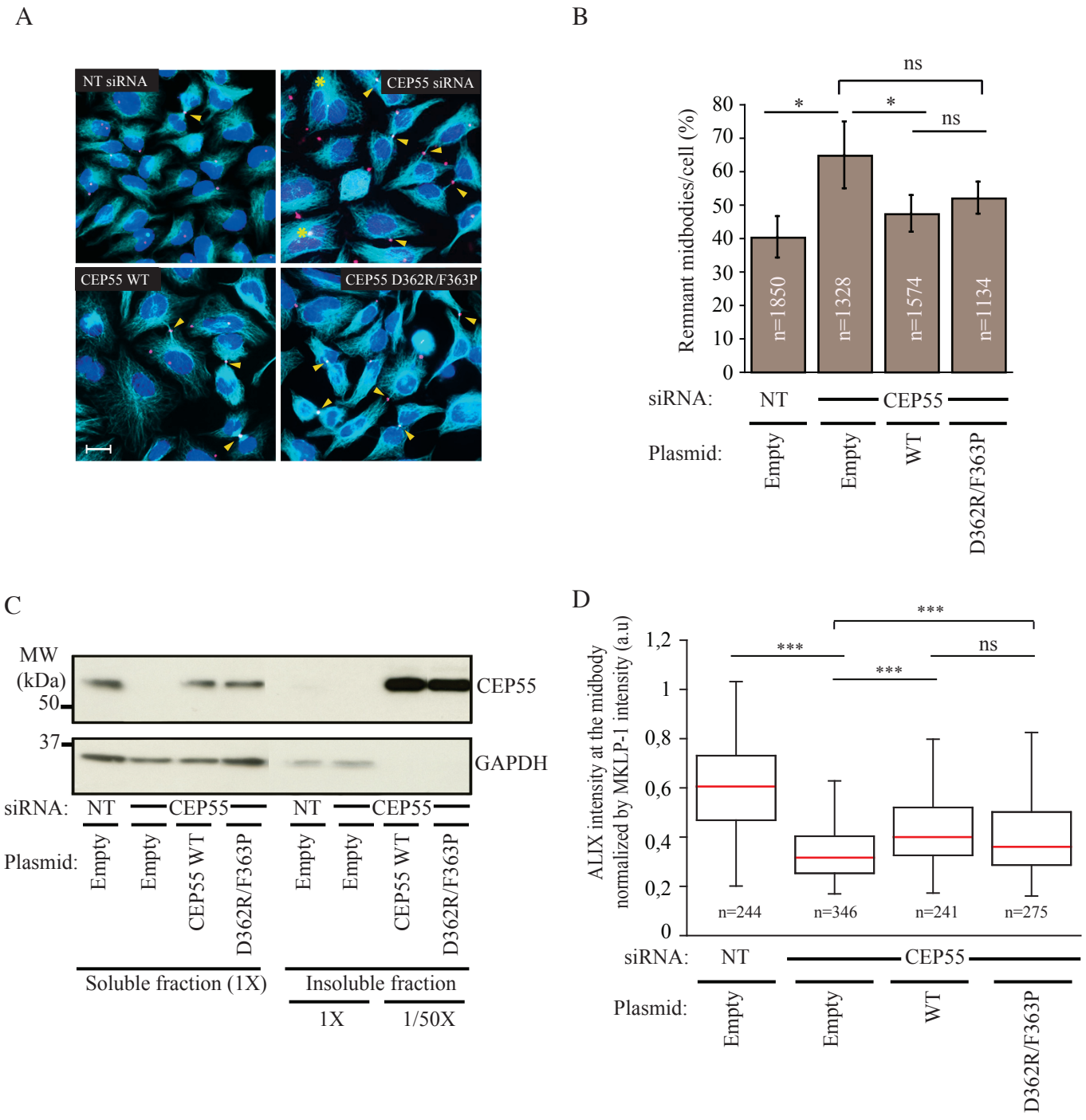
A
NT siRNA
CEP55 siRNA
CEP55 WT
CEP55 D362R/F363P
B
Remnant midbodies/cell (%)
n=1850
n=1328
n=1574
n=1134
siRNA:
NT
CEP55
Plasmid:
Empty
Empty
WT
D362R/F363P
C
MW (kDa)
50
37
CEP55
GAPDH
siRNA:
NT
CEP55
Plasmid:
Empty
CEP55 WT
D362R/F363P
Soluble fraction (1X)
Insoluble fraction
1X
1/50X
D
ALIX intensity at the midbody normalized by MKLP-1 intensity (a.u)
n=244
n=346
n=241
n=275
ns
***

Figure S6. CEP55 NOA is not involved in CEP55 recruitment to the midbody, but is absolutely required to ensure proper abscission, Related to Figure 6

HeLa cells were concomitantly transfected with a non targeting (NT) or CEP55 siRNA and with an empty vector or a CEP55 siRNA resistant vector encoding either HA-CEP55 WT or HA-CEP55 D362R/F363P.

(A) Cells were fixed with DAPI (blue), MKLP-1 (red) and β-tubulin (cyan) antibodies. Arrows and stars represent cells connected by a midbody and multinucleated cells, respectively. Quantification is represented in Figure 6 (A-B). Scale bar = 10 μM.

(B) Analysis of the D362R/F363P mutant ability to rescue midbody remnant clearance defect induced by CEP55 depletion. The exact same images as in (A) were used to quantify the ratio of midbody remnant per cell (%) as described in the experimental procedure. Data represent the mean ± SD of three independent experiments and the total number of nuclei (n) counted in the 3 experiments is indicated.

(C) Level of protein expression in the different conditions in the soluble and insoluble fractions in Figure 6 was analyzed by western blot showing a similar level of expression between the different ectopic proteins, which are mainly expressed in the insoluble fraction.

(D) Quantitative analysis of ALIX intensity at the midbody in different indicated conditions. Cells were stained with DAPI, ALIX, MKLP-1 and β-tubulin antibodies. ALIX intensity was normalized by MKLP-1 intensity at the midbody upon MKLP-1 dots. The total numbers of midbodies (n) detected are indicated.

***$p < 0.001$; *$p < 0.05$; ns: not significant ($p \geq 0.05$).

FIGURE S7

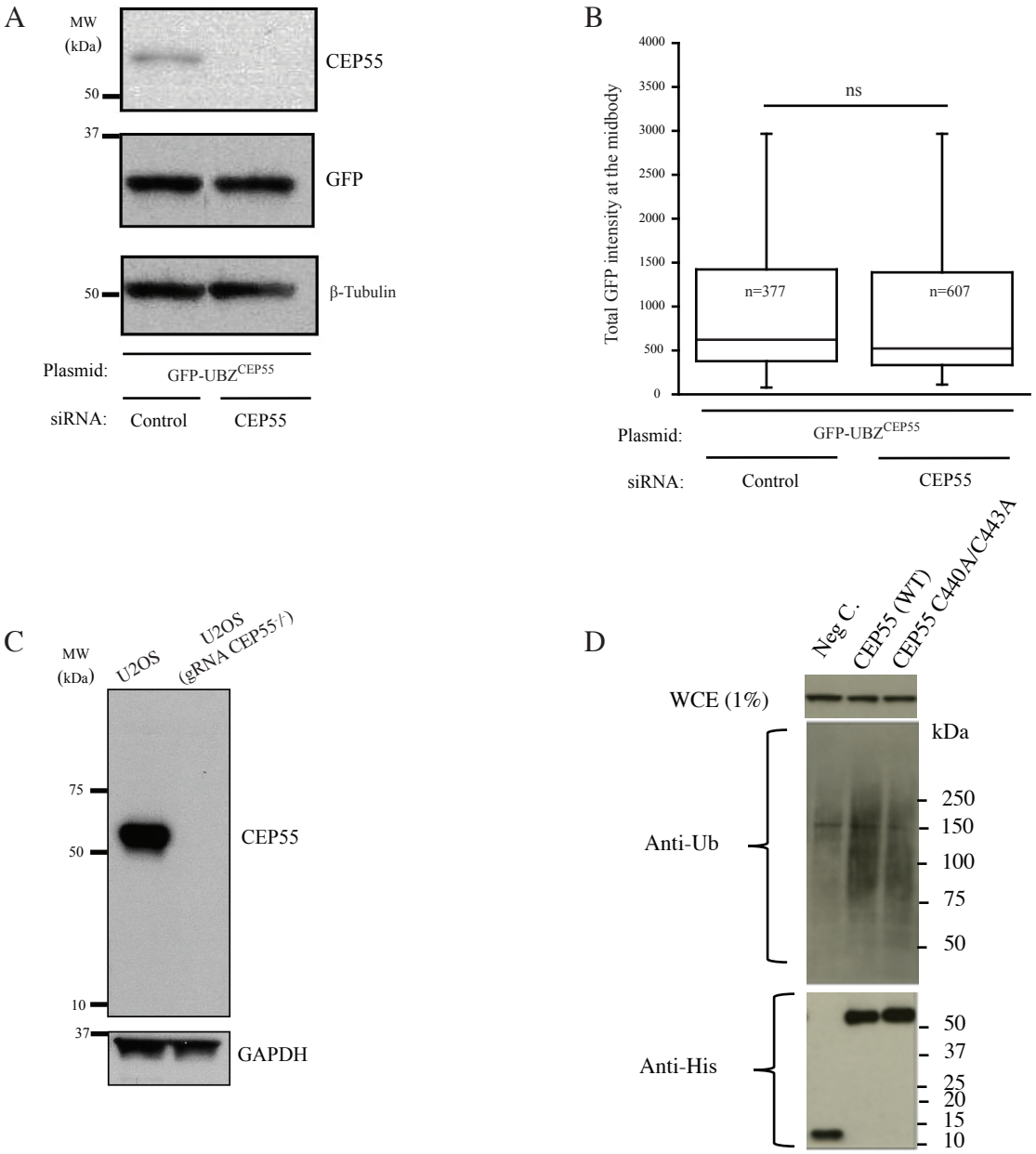
A
MW (kDa)
50
37
CEP55
GFP
50
β-Tubulin
Plasmid:
GFP-UBZCEP55
siRNA:
Control
CEP55
B
Total GFP intensity at the midbody
4000
3500
3000
2500
2000
1500
1000
500
0
ns
n=377
n=607
Plasmid:
GFP-UBZCEP55
siRNA:
Control
CEP55
C
MW (kDa)
U2OS
U2OS (gRNA CEP55-/-)
75
50
10
37
CEP55
GAPDH
D
Neg C.
CEP55 (WT)
CEP55 C440A/C443A
WCE (1%)
kDa
Anti-Ub
250
150
100
75
50
Anti-His
50
37
25
20
15
10
E
Poly-Ub (FK2)
CEP55
Merge
10µm
Tubulin
DAPI

Figure S7. The autonomous cargo receptor activity of CEP55 UBZ^{CEP55} contributes to CEP55 binding to free and anchored cellular polyubiquitin chains, and CEP55 colocalizes with polyubiquitin chains to the midbody, Related to Figure 7

(A-C) GFP-UBZ^{CEP55}exhibits an autonomous cargo receptor activity to the midbody, which is independent of endogenous CEP55. HeLa cells were concomitantly transfected with GFP-UBZ^{CEP55} and CEP55 siRNA before being analyzed by immunoblotting and fluorescence microscopy. (A) CEP55 and GFP-UBZ^{CEP55} expression levels were quantified by western blot. (B) Total GFP intensities at the midbody were quantified using MKLP-1 immunolabeling as midbody marker. The total numbers of midbodies (n) detected in two independent experiments are indicated. ns: not significant ($p \geq 0.05$). (C) Level of expression of CEP55 in parental and CRISPR-Cas9-mediated CEP55 knockout U2OS cell lines (gRNA CEP55$^{-/-}$) by western blot. GAPDH was used as loading control.

(D) The C440A/C443A debilitating UBZ^{CEP55} mutant exhibits a ubiquitin binding defect with free and anchored cellular polyubiquitin chains. The full length His-tagged Cep55 (WT) protein and its debilitating ZF double mutant His-tagged CEP55 C440A/C443A were individually purified after transient expression in 293 HEK cells. The purified His-tagged CEP55 proteins were then immobilized on Ni-NTA beads and incubated with crude extracts prepared from HeLa cells. The resulting protein complexes were subjected to an immunoblot analysis using the indicated antibodies. The NOA/UBAN mutant domain of NEMO (D311G) defective in ubiquitin binding was used as negative control (Neg C.). WCE: whole-cell extracts revealed with anti-GAPDH showing that the same amount of WCE was incubated with beads containing either the CEP55 mutant or the WT.

(E) IF microscopy images of CEP55 (far red), polyubiquitin chains (green), tubulin (red) and nucleus (blue) and all four components (merge) at the late stage of cytokinesis in HeLa cells. Shown are representative images at 60x magnification with inset zooming into the midbody area.

TABLE S1, Related to Figures 1 and 3

Zn-induced folding of the WT and mutant (E460A) CEP55 ZF peptide				
	FRET efficiency (Tyr to Trp)			
	$-Zn^{2+}$	$+Zn^{2+}$	$+Zn^{2+}/-Zn^{2+}$	Zn stoichiometry
ZF(W) WT	0.28 ± 0.03	0.53 ± 0.03	1.9 ± 0.03	0.97 ± 0.24
ZF(W) E460A	0.37 ± 0.08	0.65 ± 0.05	1.8 ± 0.05	0.86 ± 0.04

Transparent Methods

Cell lines and cell culture

Human HeLa cells (American Type Culture Collection) were grown in DMEM supplemented with 10 % fetal bovine serum, penicillin (50 units/ml) and streptomycin (50µg/ml), while 293-F cells were grown in suspension in FreeStyle™ 293 Expression Medium (Gibco®). Human WT U2OS (American Type Culture Collection) and *Cep55*^{CrisprKO} U2OS cells were grown in the same conditions without antibiotics.

Plasmids, ZF peptides, antibodies and siRNAs

pET28 plasmids encoding human CEP55 WT His-NOA, Δ (343-364) His-NOA, L351A/Q354A/Q355A His-NOA and D362R/F363P His-NOA were purchased from GeneART (ThermoFisher sientific, MA USA). pcDNA3 plasmids (Invitrogen) encoding human HA-CEP55 WT (1-464), HA-CEP55 D362R/F363P, HA-CEP55 C440A/C443A, HA-CEP55 E460A, HA-CEP55 CEP55 D362R/F363P/C440A/C443A and the pGEX4T2-di-Ub and tetra-Ub-plasmid (GE Healthcare) encoding linear di- and tetra-ubiquitin were prepared using conventional molecular cloning and PCR mutagenesis methods. pcDNA3 plasmids encoding the human His-strep-CEP55 WT (1-464), His-strep-CEP55 C440A/C443A, His-strep-CEP55 ΔZF-UBZ^{WRNIP1}(15-53), His-strep-CEP55 ΔZF-UBZ^{RAD18} (201-240), His-strep-CEP55 ΔZF-UBZ^{NDP52}(440-470), His-strep-CEP55 ΔZF-nZF2^{TAB2} (665-693) and His-strep-CEP55 ΔZF-A20^{ZF7}(759-790), were purchased from Eurofins Genomics (France-Germany). pEGFP-C1 plasmid (Clontech) encoding GFP-ZF^{CEP55} was purchased from Eurofins Genomics (France-Germany). A pET52b3C/LIC plasmid (Merck Millipore) encoding Strep-Tag-II-tagged human ubiquitin-conjugating enzyme E2–25K-C170S was prepared by Ligation Independent Cloning following the manufacturer's instructions. pGEX-Ubc13 (18894) and pET16b- Mms2 (18893) were provided by Addgene (Cambridge, MA).

WT and E460A CEP55 ZF (W) (residues 435-464), StrepII-Tag CEP55 ZF and N-terminal fluorescein-labeled-CEP55 ZF peptides (CEP55 F-ZF) (>95% purity) were purchased from Covalab (Villeurbane, France).

Antibodies against the following proteins were used : anti-β-tubulin (T4026, Sigma), anti-α-tubulin (Homemade, Institut Curie), anti-CEP55 (sc-374051, Santa Cruz), anti MKLP-1 (sc-867, Santa Cruz), anti-GAPDH (sc-59540, Santa Cruz), anti-ALIX (3A9, Cell Signaling), anti-

TSG101(4a10, GeneTex), anti-HA II and anti-GFP. CEP55 siRNA (SI02653021, Qiagen) and Non-targeting (D-001810-10, Dharmacon) were used.

Transfections, cell-lysis and western blot

Human HeLa cells (American type Culture Collection) were grown in DMEM supplemented with 10 % fetal bovine serum, penicillin (50 units/ml) and streptomycin (50µg/ ml). Human U20S WT (American Type Culture Collection) and U20S K.O CEP55-/- were grown in the same conditions without antibiotics.

For functional complementation experiments with HA-CEP55 plasmids, HeLa cells were first seeded in 6 well dishes and extemporaneously transfected with the siRNAs. After 24 h, cells were washed in DMEM and transfected with 1 µg of the different plasmids. 24 h later cells were briefly trypsined before being seeded and transfected a second time with the siRNAs. Cells were fixed and imaged or lysed for western blot 96 h post 1st siRNA transfection. For GFP and GFP-ZF^{CEP55} transfections, HeLa cells were seeded with or without siRNAs and transfected 9 hours later with 2 and 0.5 µg of plasmids in 6 wells or in 24 wells, respectively. Cells were fixed in PFA 4% or lysed 40 h post-transfection. *Cep55^{CrisprKO}* and WT U2OS cells were transfected in a 6 well dishes with 200 ng of the different plasmids upon 1µg of total DNA (50 ng / 250 ng total DNA for a 24 well) before being fixed in methanol 100% or lysed 48h post-transfection.

For all siRNA transfections, HiPerFect (Qiagen) was used to transfect N-T or CEP55 siRNA (24 nM) according to manufacturer's instructions. FuGENE HD (Promega) was used for all DNA transfections according to manufacturer's instructions.

HeLa cells were lysed on ice in a RIPA buffer containing 50 mM Tris HCl pH 7,2, 150 mM NaCl, 5mM EDTA, 0,1% SDS, 1% Deoxycholate,1% Triton X100 and a mixture of protease inhibitors (Complete, Roche) for 35 min at 4°C. Lysates were centrifuged at 17000 x g for 15 min. Supernatants (soluble fraction) were mixed with 4X XT Sample buffer (Biorad) and 50 mM DTT and pellets (insoluble fraction) were solubilized in Sample buffer before being boiled for 10 min. U20S cells were directly lysed in XT Sample buffer and boiled during 10 min.

Proteins were separated by SDS-PAGE and transferred to PVDF membranes. Immunoreactive proteins were visualized by chemiluminescence.

Generation of *Cep55^{CrisprKO}* U2OS cells

The U2OS CEP55 KO cell line was generated using Santa Cruz Biotechnology CRISPR systems according to the manufacturer instructions. Briefly, this CRISPR/Cas9 system relies on the use of three gRNAs designed against CEP55 exon 3 and exon 5 (target sequence non-provided) and the use of RFP Puromycin resistance DNA donor with two 800 bp long homologous arms. 50 000 U2OS cells were transfected with 0.1 µg of gRNAs plasmid, 0.1ug of RFP DNA donor and 0.1 µg of Cas9 plasmid using 2.4 µl of Fugene HD (Promega). After 72 h, Puromycin was added in the medium (1 µg/mL) for 72 h, then cells were sorted by FACS in order to obtain a single red cell per well. Targeted loci were finally amplified by PCR for each isolated clone and sequenced to validate a successful knockout (oligo and clone sequences available upon request).

Pull-down experiments assays

50 μl of purified CEP55 His-NOA and His-Darpin (used as a negative control) at 8 μM in Tris-HCL 20 mM, pH 8, KCl 50 mM, DDM 0.2 mM, Imidazol 10 mM, Glycerol 10% were incubated for 1h at room temperature with nickel-nitrilotriacetic acid magnetic beads (12 μl, Invitrogen) which were pre-equilibrated in the protein buffer. The beads were washed 3 times in protein buffer and incubated for 1h at 4°C with increasing concentrations of linear or Lys-63 tetra-ubiquitin (1-2-4-8-16 μM) in the same buffer. His-darpin was incubated with the highest ubiquitin concentration tested (16 μM). Three fast washes were then performed at 4°C and the complexes were directly eluted in Sample Buffer in presence of 50 mM DTT before being boiled and analyzed by SDS-PAGE followed by a Coomassie blue staining.

For the linear, Lys-63, Lys-11, Lys-48 tetra-ubiquitin pull-down assay, 16 μM of various ubiquitins were incubated with CEP55 His-NOA and His-Darpin (8 μM) was incubated with 16 μM of linear tetra-ubiquitin.

Immunofluorescence, imaging and quantification

For methanol fixation, cells cultured on glass coverslips were fixed with 100% methanol at 4°C. Cells were progressively rehydrated by successive washes with 85%, 70%, and 50% ethanol in water and two final washes with PBS. For PFA fixation, cells cultured on glass coverslips were fixed with PFA 4% as previously described in Lobry et al., 2007.

After blocking by incubation with 1% BSA in PBS, the slides were incubated with the primary antibodies, washed, and incubated with species-specific fluorochrome-tagged secondary antibodies. They were washed again and incubated with DAPI (Sigma-Aldrich) to

stain the nuclei. The coverslips were mounted in Mowiol and were examined with an ApoTome imaging system (Imager Z1) equipped with a 63×/1.4 NA oil differential interference contrast (DIC) objective lens (all from Carl Zeiss). Images were acquired and analyzed with AxioVision software (Carl Zeiss).

For the quantification of the percentage of cells connected by midbodies (%cell-mid), multinucleated cells (%multi) and remnant midbodies/cell (%rem/cell), the different conditions were blind counted. The total number of nuclei (Nnuc) and mibodies (Nmid) were automaticaly counted using Icy (De Chaumont et al., 2012) by detecting DAPI stainings and MKLP-1 dots respectievly. The number of multinucleated cells (Nmulti) and cells connected by midbodies (Ncell-mid) in the different conditions were manualy counted. The total number of cells (Ncells), the percentage of cells connected by midbodies, of multinucleated cells and of remnant midbodies/cell were calculated as follow : Ncells = Nnuc-(Nmulti+Ncell-mid) ; %cell-mid = (Ncell-mid/Ncells) x 100 ; %multi = (Nmulti/Ncells) x 100 ; %rem/cell = (Nmid- Ncell-mid)/Ncells.

For the quantification of CEP55 intensity at the midbody, the midbodies (MKLP-1 positive dots) were detected using spot detector on Icy and were defined as regions of interest. The CEP55, ALIX and MKLP-1 intensities in these regions of interest were determined on Icy and the CEP55 and ALIX intensites at the midbody were normalized by MKLP-1's.

For the quantification of the percentage of recruitment to the midbody (% recruitment Mid) of the different CEP55 proteins in CEP55-/- U20S cells lines, we used a colocalizer script on Icy. It detects the total dots of MKLP-1 (MKLP-1 dots) and of CEP55 in cells and the colocalized dots (Coloc Dots). The percentage of recruitment was calculated as follow : % recruitment Mid = Coloc Dots / MKLP-1 dots * 100. Relative percentages of recruitments of the different CEP55 proteins compared to WT were then calculated. The percentage of recruitment of GFP or GFP-ZF^{CEP55} to the midbody was calculated in the same way but specifically in visually transfected cells.

Purification of various proteins and ubiquitin expression

Protein purification of all the proteins was carried out on a ÄKTA Prime Purifier (Amersham Pharmacia Biotech). Ubc13, linear di-ub and tetra-Ub expressed as a glutathione-S-transferase (GST) fusion protein, StrepTagII-E2–25K-C170S, His-Mms2 were purified and Lys-63 di-Ub , Lys-63 and Lys-48 tetra-Ub were enzymatically produced as previously described in (Ngadjeua et al., 2013). Commercial available K11 tetra-ub (Lifesensor) was used. His-Darpin was purified as described in (Wyler et al., 2007). NEMO His-NOA and WT/mutants CEP55

His-NOA were purified from insoluble bacterial extracts and solubilized by 8M urea in 50 mM Tris-HCl, pH 8.0, 1M NaCl, 0.5 mM TCEP. Proteins were directly renaturated on the Ni-NTA resin (Qiagen) by applying a reverse, linear urea gradient (8 to 0 M urea) before being eluted in 1M imidazol and dialysed against a 50 mM Tris-HCl, pH 8.0, 500 mM NaCl, 0.2 mM TCEP buffer. WT CEP55 GST-NOA was purified from insoluble bacterial extracts and solubilized at room temperature by 10 % Sarkosyl in 50 mM Tris-HCl, pH 8.0, 300 mM NaCl, 0.1 mM TCEP. The Sarkosyl was then diluted (2%) in a 50 mM Tris-HCl, pH 8.0, 300 mM NaCl, 0.1 mM TCEP, 30 mM CHAPS, 3% Triton X100 and the protein was purified with glutathione Sepharose 4B column (GEHealthcare) according to the manufacturer's instructions. The protein was then dialyzed against a 50 mM Tris-HCl, pH 8.0, 300 mM NaCl, 0.1 mM TCEP, 0.5 DDM buffer. After purification, all proteins were concentrated and stored at -80 °C.

Purification of the WT full-length CEP55 and its C440A/C443A debilitating ZF mutant in human cells, and poly-Ub binding assay

293-F human cells ($2.4x10^9$) were transiently transfected with pcDNA3.1/His-strep-CEP55 WT (1-464) or its double mutant (C440A/C443A). Seventy-two hours after transfection, cells were lysed in LB buffer (50 mM Tris-HCl, pH 8.0, 50 mM NaCl, 2 mM $MgCl_2$, 1% Triton X100, 15% glycerol, 0.1 mM TCEP) containing 40 u/ml Benzonase (Millipore) with an EDTA-free protease inhibitor mixture (Sigma-Aldrich). After centrifugation at 15,000 x g for 15 min at 4°C, the recovered pellet was washed twice with WB buffer (50 mM Tris-HCl, pH 8.0, 500 mM NaCl, 0.1 mM TCEP) containing 0.5 mM dodecyl maltoside (DDM) before solubilization with DB denaturation buffer (50 mM Tris-HCl, pH 8.0, 1 M NaCl, 0.1 mM TCEP, 10 mM imidazole) containing 8 M urea. The denatured pellet was then diluted three times with WB buffer and incubated with Ni-NTA superflow beads (2ml, Qiagen) overnight at room temperature. After two washes with DB buffer, the immobilized His-tagged proteins were renatured by incubating beads with RB renaturation buffer (DB buffer without urea) at 4°C overnight. Following extensive washing of six bed volumes of beads in RB buffer (12 ml), the WT full length His-tagged CEP55 and its C440A/C443A ZF double mutant were at least 95% homogenous as judged by SDS-PAGE analysis with Coomassie blue staining (stained gel available upon request). The immobilized CEP55 proteins were then stored at -20°C after equilibrating beads with buffer SB (50 mM Tris-HCl, pH 8.0, 500 mM NaCl, 0.2 mM TCEP) containing 50% glycerol. Protein concentrations were determined by densitometry according to the intensity of polypeptide bands stained with Coomassie blue and using BSA as reference.

For poly-Ub binding assay, HeLa cells (36 x 10^6) were lysed in LBB buffer (50 mM Tris-HCl, pH 7.5, 50 mM NaCl, 2 mM $MgCl_2$, 1% Triton X100, 10% glycerol, 0.5 mM TCEP, 10 mM imidazole) containing an EDTA-free protease inhibitor mixture with the PR619 deubiquitinase inhibitor (5 μM) and a phosphatase inhibitor cocktail (PhosSTOP, Sigma-Aldrich). After centrifugation at 15 000 x g for 10 min at 4°C, the clarified cell lysate was then divided in three parts and each part was incubated overnight at 4°C with 20 μg of the purified WT full-length His-tagged CEP55, the debilitating ZF double mutant or the NOA/UBAN mutant domain of NEMO (D311G, negative control) immobilized on Ni-NTA beads (50 μl). The beads were then washed three times with LBU buffer, and bound polyubiquitin chains were detected by western blot using an anti-ubiquitin antibody (P4D1, Enzo Life Sciences).

Size exclusion chromatography - multi angle light scattering (SEC-MALS) analysis

The analysis were carried out on a ÄKTA purifier on a column of gel-filtration Superdex 200 (GE-Healthcare) coupled to a multi angle light scattering detector DAWN-HELEOS and a refractometer Optilab rEX (Wyatt Technology, USA) at room temperature.

The WT, Δ (343-364), L351A/Q354A/Q355A, D362R/F363P His-NOA were filtred on 0.22 μM filters in Tris-HCL 20 mM, pH 7.5, NaCl 600 mM, DTE 0.2 mM and 500 μl of each protein (20 μM) were injected. Unicorn software was used to pilot the size exclusion chromatography and ASTRA VI. The normalization of the peaks and the band broadening were performed using Bovin Serum Albumin. Toluen was used to calibrate the 90° scattered light.

SDS-PAGE in reducing or non-reducing conditions

Sample buffer (4X) containing or not 100 mM DTT was added to 3 µg of CEP55 WT, Δ (343-364), L351A/Q354A/Q355A, D362R/F363P His-NOA in 50 mM Tris-HCl, pH 8.0, 500 mM NaCl, 0.2 mM TCEP. Samples were boiled during 10 min and analysed by SDS-PAGE.

BLI experiments

Biolayer interferometry (BLI) experiments were performed on a BLItz system (Fortebio) at room temperature. GST-ub2 M1 (20μM) was immobilized on anti-GST biosensors (Fortebio) in Tris HCL 50 mM, pH 8, NaCl 150 mM, TCEP 0.1 mM which were pre-equilibrated in the same buffer. The biosensors were then incubated with Tris HCL 50 mM, pH 8, NaCl 150 mM, TCEP 0.1 mM, $ZnCl_2$ 1 mM before adding various concentrations of Strep-tag-II WT ZF CEP55 (25-12.5-6.25-1 μM) and E460A ZF CEP55 (25-12.5-6.25 μM) which were prefolded in the same buffer in 1mM Zncl2 during 5 min at room temperature. The dissociation of the

complexes on the biosensors was performed by incubating them in the peptide free buffer. Lys-63 Ub2-7 (0.2 mg/ml) was immobilized on SA-streptavidin biosensors (Fortebio) before adding various concentrations of WT strep-tag-II ZF CEP55 (20-10-5-1 μM) in Tris HCL 50 mM, pH 8, NaCl 150 mM, TCEP 0.1 mM, $ZnCl_2$ 100 nM which were prefolded in the same buffer during 5 min at room temperature. For the biotin Lys-48 Ub2-7 /Strep-tag-II -WT ZF CEP55 binding assay, Lys-48 Ub2-7 (0.2 mg/ml) was immobilized on biosensor before adding 10 μM of Strep-tag-II -WT ZF CEP55.

For the CEP55 WT, Δ (343-364), L351A/Q354A/Q355A, D362R/F363P HIS-NOA binding assay with linear tetra-ubiquitin, His-NOA proteins (8μM) were immobilized on anti-penta-His biosensors (Fortebio) in Tris HCL 50 mM, pH 7.5, NaCl 150 mM, TCEP 0.2 mM. Various concentrations of linear tetra-ubiquitin were then incubated with the proteins (20-10-5-2.5 μM for WT His-NOA and 5-2.5 μM for the mutants). The dissociation of the complexes on the biosensors was performed by incubating them in the protein free buffer. Steady state analysis in Data Analysis BLItz version 1.2 (Fortebio) was used to calculate the K_D.

Zinc ion colorimetric titration assay

To determine the zinc content of the WT and E460A ZF (W), a colorimetric 4-(2-pyridylazo) resorcinol metal binding assay was used (PAR colorimetric assay). Briefly, the WT and E460A synthetic peptides were first refolded for 1 h in TrisHCL 50 mM, pH 7.5, NaCl 150mM, TCEP 0.1 mM and 2mM $ZnCl_2$, and abundantly dialyzed against the same buffer without $ZnCl_2$ to remove unbound zinc. Protein samples (5–15-25μM) were then incubated for 30 min at room temperature with proteinase K (0.1 mg/ml) to completely release the zinc ion before adding 4-(2-pyridylazo)resorcinol (200 μM). The amount of the released zinc was determined quantifying the (4-(2-pyridylazo)resorcinol)$_2$-Zn^{2+} complex at 492 nm from a calibration curve, calculated from known concentrations of $ZnCl_2$.

Circular dichroism spectroscopy

Circular dichroism (CD) experiment was carried out with an Aviv 215 polarimeter (Aviv Instruments, Lakewood, NJ), with a 20 mm path-length parallelepipedic quartz cell. Before analysis, the purified His-NOA was extensively dialyzed against a TrisHCl 25 mM, pH 7.5, NaCl 150mM, TCEP 1 mM, NaF 200 mM buffer and its concentration was adjusted to 20 μM. The exact concentration was determined after the CD experiment, by amino-acid analysis. Far-UV CD spectrum was recorded at room temperature, from 185 to 260 nm, at 1 nm intervals, and the spectrum generated is the mean of three scans minus the mean of three scans of the

reference buffer. Data were normalized as follows: $\theta norm = \theta/(Lp \times 3298 \times 10 \times Lc \times C)$, where $\theta norm$ is the normalized CD signal, θ is the CD signal before normalization (mdegrees), Lp is the number of peptide bonds, Lc is the path length and C the molar concentration of protein. The α-helical content of each protein was determined from the CD signal at 222, 208 and 191 nm, by the equation $\%H = ((\theta norm - \theta 0\%)/(\theta 100\% - \theta 0\%)) \times 100$ where $\theta 0\%$ and $\theta 100\%$ are signals of reference peptides at 0 and 100% of helicity respectively.

Fluorescence spectroscopy and determination of internal FRET efficiency

Fluorescence measurements for both WT and E460A ZF (W) peptides were recorded on a PTI multimodular QuantaMaster spectrofluorimeter (PTI,Lawrenceville, NJ) at room temperature. The peptides (300μM) were folded in 50mM Tris HCl, pH 7.5, 150 mM NaCl, 0.1 μM TCEP, 2mM $ZnCl_2$ and then dialysed against the same free $ZnCl_2$ buffer to remove $ZnCl_2$ excess.

Emission spectra (300-450 nm) of the folded and unfolded peptides (2μM) were measured at an excitation wavelength of 280 nm excitating both the tyrosines and the tryptophan. Emission spectra from dialysis buffer were subtracted to the spectra obtained.

To determine the internal FRET from tyrosines to tryptophan into the folded and unfolded ZF (W) peptides, the tryptophan emissions (350 nm) and the absorbances of the peptides (5 μM) at 275, 285 and 290 nm were measured. The experimental tryptophan quantum yields (Q_{exp}) were calculated for the 3 wavelengths. The experimental relative tryptophan quantum yields (Qr_{exp}) were then obtained by the relation $Qr_{exp}(\lambda ex) = Q_{exp}(\lambda ex)/ Q_{exp}(\lambda_{ex=290nm})$ assuming that at 290 nm the absorbance of tyrosines are negligible compared to tryptophan's. The theoretical relation used to determine the FRET efficiency is $Qr_T(\lambda ex) = F_{trp}(\lambda ex) + E \times F_{tyr}(\lambda ex)$ (Eisinger, 1969) with E the FRET efficiency, $Qr_T(\lambda ex)$ the theoretical relative tryptophan quantum yield, $F_{trp}(\lambda ex)$ and $F_{tyr}(\lambda ex)$ the theoretical fractional absorbances of tryptophan and tyrosine respectively for a 1Trp/2tyr ratio, at a fixed excitation wavelength (λex). $F_{trp}(\lambda ex)$ and $F_{tyr}(\lambda ex)$ were determined using molar extinction coefficients of tyrosine and tryptophan ε_{tyr} and ε_{trp} available online http://omlc.org/spectra/PhotochemCAD/html/091.html and http://omlc.org/spectra/PhotochemCAD/html/092.html respectively (Dixon et al., 2005) as the following equation: $F_{tyr}(\lambda ex) = 2 \times \varepsilon_{tyr}(\lambda ex)/(2 \times \varepsilon_{tyr}(\lambda ex) + \varepsilon_{trp}(\lambda ex))$ and $F_{trp}(\lambda ex) = \varepsilon_{tyr}(\lambda ex)/ (2 \times \varepsilon_{tyr}(\lambda ex) + \varepsilon_{trp}(\lambda ex))$. The experimental relative tryptophan quantum yields (Qr_{exp}) were then reported on the $Qr_T(\lambda ex)$ curves (not-shown) and the FRET efficiency from tyrosines to tryptophan into the peptides were determined.

To estimate the affinity of CEP55 ZF(W) WT and E460A for zinc, each peptide was titrated adding increasing concentrations of $ZnCl_2$ at an excitation and an emission wavelength of 280 and 342 nm respectively. Data were fitted using a quadratic equation as followed: $X_{bound} = (K_D + n \times Cp + C_{ZN} - ((K_D + n \times Cp + C_{ZN})^2 - 4n \times Cp \times Czn)^{1/2}) / 2n \times Cp$ where X_{bound} is the peptide fraction bound to zinc, Cp and C_{ZN} the total peptide and zinc concentrations, K_D and n the dissociation constant and the stoichiometry of the peptide-zinc complex. X_{bound} was determined by the following equation: $X_{bound} = (F_{obs}-F_0) / (F_{max}-F_0)$ where F_{obs} is the observed fluoresence, F_0 and F_{max} the fluorescence in absence and in presence of saturating concentration of zinc respectively.

Fluorescence polarization experiments

Fluorescence polarization (FP) experiments measurements were recorded on a Tecan microplate reader infiniteR F500 (Tecan France S.A.S) at 25°C using a 485-nm excitation filter and a 535-nm emission filter in a binding buffer (Tris HCl 50 mM, pH 7.5, NaCl 150mM, TCEP 0.1 mM, DDM 0.2mM) in the presence or absence of 1mM $ZnCl_2$. The fluorescein labelled peptides WT and E460A F-ZF (0,5µM) were titrated with increasing concentrations of mono-ubiquitin from 0 to 1000 µM. To assess non-specific binding, similar experiments were performed in the absence of $ZnCl_2$ with unfolded peptides. Under these latter conditions the deviations of the FP signals, which vary linearly with ubiquitin concentration, can be fitted according to a linear function with slopes of 0.04 and 0.02 mP/µM for WT and E460A F-ZF respectively. This non-specific component was subtracted from the FP data obtained in presence of $ZnCl_2$. Curve fitting of the FP data was then done by nonlinear regression using the equation $P_{obs} = (P_{max}-P_0) \times Ubi/(K_D+ubi) + P_0$ to solve the dissociation constant K_D given P_{obs} (Polarization at a given concentration of ubiquitin), P_{max} (polarization after saturation with ubiquitin), P_0 (polarization in the absence of ubiquitin), Ubi (ubiquitin concentration). To check the contribution of $ZnCl_2$ in the binding between F-ZF peptide and ubiquitin, the same experiment was performed with a pre-folded ZF WT in the absence of $ZnCl_2$ in the binding assay. The peptide was pre-folded in TrisHCL 50 mM, pH 7.5, NaCl 150mM, TCEP 0.1 mM, $ZnCl_2$ 10 mM and dialysed against the same free $ZnCl_2$ buffer to remove $ZnCl_2$ excess. The same protocol was applied to the unfolded WT F-ZF without $ZnCl_2$. The folded and unfolded peptides were then titrated by ubiquitin. A similar K_D than for the condition containing $ZnCl_2$ in the binding buffer was obtained (data not-shown).

CEP55 F-ZF WT titration by Lys-63 di-ubiquitin (0-500 µM) was performed in 0.2 mM $ZnCl_2$. An isodesmic increase of fluorescence polarization was observed for high concentration

of ubiquitin (100-500 µM) and the contribution of this non-specific binding (Ns) was estimated using $P_{obs}= (P_{max}-P_0) \times Ubi/(K_D+ubi) +Ns \times Ubi + P_0$. This non-specific component (N_S) was then subtracted to the data and the curve was fitted as for mono-ubiquitin titration.

Structural modeling

The model of CEP55 ZF in interaction with mono-ubiquitin was generated by homology modeling. The structural model of CEP55 ZF apoform was first generated on the basis of the NMR model of NEMO ZF (2JVX) using the free access server Swiss-model (Arnold et al., 2006). The model quality was estimated using the Anolea, and verify3D programs, which are available in the Swiss-model worksplace and the geometry of the residues was evaluated using the Procheck software (Laskowski et al., 1993). Co-crystal structure of the GFP - ZF WRNIP1 (Werner helicase interacting protein 1) in interaction with mono-ubiquitin (PDB ID : 3VHT) was used as a template for the modelization of CEP55 ZF in interaction with ubiquitin. The complex was modelized by molecular replacement superimposing the Cα of CEP55 ZF with WRNIP1 ZF and a energy minimization of the complex was carried out using the force fields GROMOS96 (van Gunsteren et al., 1996).

The semi-flexible refinement of the interface between ZF CEP55 and ubiquitin was then performed by simulated annealing using the standard protocols implemented in HADDOCK (de Vries et al., 2010).The models of CEP55 NOA in interaction with linear di-ubiquitin and with K63 di-ubiquitin were generated according to the same procedure than the ZF model. Briefly, structural model of CEP55 NOA apoform was generated using the free H2O and free ubiquitin co-cristal structure of NEMO NOA in interaction with linear di-ubiquitin (PDB ID : 2ZVO). The semi-flexible refinement of the interface between the two monomers into the apo CEP55 NOA coiled coil was performed by simulated annealing using HADDOCK software. The co-crystal structures of NEMO NOA in interaction with M1- (PDB ID : 2ZVO) or K63-linked (PDB ID : 3JSV) di-ubiquitin were then used as templates and a refinement of the interfaces were carried out.

Quantification and statistical analysis

Statistical analyses were performed in Kaleidagraph (4.5.2.). The non-parametric Kruskal-Wallis test was used to determine statistical significance.

Supplemental References

ARNOLD, K., BORDOLI, L., KOPP, J. & SCHWEDE, T. 2006. The SWISS-MODEL workspace: a web-based environment for protein structure homology modelling. *Bioinformatics,* 22**,** 195-201.

DE CHAUMONT, F., DALLONGEVILLE, S., CHENOUARD, N., HERVE, N., POP, S., PROVOOST, T., MEAS-YEDID, V., PANKAJAKSHAN, P., LECOMTE, T., LE MONTAGNER, Y., LAGACHE, T., DUFOUR, A. & OLIVO-MARIN, J. C. 2012. Icy: an open bioimage informatics platform for extended reproducible research. *Nat Methods,* 9**,** 690-6.

DE VRIES, S. J., VAN DIJK, M. & BONVIN, A. M. 2010. The HADDOCK web server for data-driven biomolecular docking. *Nat Protoc,* 5**,** 883-97.

DIXON, J. M., TANIGUCHI, M. & LINDSEY, J. S. 2005. PhotochemCAD 2: a refined program with accompanying spectral databases for photochemical calculations. *Photochem Photobiol,* 81**,** 212-3.

EISINGER, J. 1969. Intramolecular energy transfer in adrenocorticotropin. *Biochemistry,* 8**,** 3902-8.

LASKOWSKI, R. A., MACARTHUR, M. W., MOSS, D. S. & THORNTON, J. M. 1993. PROCHECK-a program to check the stereochemical quality of protein structures. *Journal of Applied Crystallography,* 26**,** 283-291.

LOBRY, C., LOPEZ, T., ISRAEL, A. & WEIL, R. 2007. Negative feedback loop in T cell activation through IkappaB kinase-induced phosphorylation and degradation of Bcl10. *Proc Natl Acad Sci U S A,* 104**,** 908-13.

VAN GUNSTEREN, W. F., BILLETER, S. R., EISING, A. A., HÜNENBERGER, P. H., KRÜGER, P., MARK, A. E., SCOTT, W. R. P. & TIRONI, I. G. 1996. *Biomolecular simulation: the GROMOS manual and user guide,* ETH Zürich, Switzerland:vdf Hochschulverlag.

WYLER, E., KAMINSKA, M., COIC, Y. M., BALEUX, F., VERON, M. & AGOU, F. 2007. Inhibition of NF-kappaB activation with designed ankyrin-repeat proteins targeting the ubiquitin-binding/oligomerization domain of NEMO. *Protein Sci,* 16**,** 2013-22.

KEY RESOURCES TABLE

REAGENT or RESOURCE	SOURCE	IDENTIFIER
Antibodies		
Mouse monoclonal anti β-tubulin (clone 2.1)	Sigma-Aldrich	Cat# T4026
Mouse monoclonal anti-CEP55 (clone B8)	Santa-Cruz Biotechnology	Cat# sc-374051
Rabbit polyclonal anti-MKLP-1 (clone N-19)	Santa-Cruz Biotechnology	Cat# sc-867
Mouse monoclonal anti-GAPDH (clone 1D4)	Santa-Cruz Biotechnology	Cat# sc-59540
Rabbit polyclonal anti-CEP55	Sigma-Aldrich	Cat# HPA023430
Human anti-α-tubulin	Homemade, Institut Curie	A-R-H#2
Mouse monoclonal anti-ALIX (clone 3A9)	Cell Signaling	Cat# 2171
Mouse monoclonal anti-TSG101 (clone 4a10)	GeneTex	Cat# GTX70255
Mouse monoclonal anti-HA 11 (clone 16B12)	Covance	Cat#MMS-101P
Mouse monoclonal anti GFP (clone 7.1)	Roche	Cat# 11814460001
Mouse monoclonal anti-polyubiquitin chains (FK2)	Enzo Life Sciences	Cat#PW8810
Mouse monoclonal antibody (P4D1)	Enzo Life Sciences	Cat#PW0930
Goat anti-IGG1 Mouse A488	Invitrogen	Cat#A-21121
Goat anti-IGG2A Mouse A546	Invitrogen	Cat#A-21133
Goat anti-IGG Mouse A488	Invitrogen	Cat#A-11029
Goat anti-IGG Rabbit A647	Invitrogen	Cat#A-21245
HRP Horse anti-Mouse IgG Antibody	Invitrogen	Cat#PI-2000
HRP Horse anti-Rabbit IgG Antibody	Invitrogen	Cat# PI-1000
Chemicals, Peptides, and Recombinant Proteins		
PBS 1X	Gibco	Cat #14190169
Trypsin	Gibco	Cat #25300
Fœtal Bovine serum	Lonza	Cat#DE14-801F
DMEM	Gibco	Cat #31966047
Penicillin/streptomycin	Gibco	Cat #15140148

Continued

REAGENT or RESOURCE	SOURCE	IDENTIFIER
Ampicillin	Sigma-Aldrich	Cat#A9518
Puromycin dihydrochloride	Euromedex	Cat#UP9200
Kanamycin Sulfate	Roche	Cat#106801
Roche cOmplete™ , EDTA-free protease inhibitors	Sigma-Aldrich	Cat#4693132001
Roche phosSTOP™ inhibitor cocktail	Sigma-Aldrich	Cat#4906845001
XT Sample buffer (4X)	Bio-Rad	Cat#1610791
FuGENE HD	Promega	Cat#E2311
HiPerFect	Qiagen	Cat#301705
PEIpro®	Polyplus (France)	Cat#115-040
DAPI	Invitrogen	Cat #D3571
PFA	Alfa aesar	Cat #30525-89-4
Methanol	Sigma-Aldrich	Cat #32213
Mowiol	Fluka	Cat #81381
4-(2-pyridylazo)resorcinol	Sigma-Aldrich	Cat#323209
Benzonase® nuclease	Millipore (Merck)	Cat#70664
PR-619, DUB inhibitor	Sigma-Aldrich	Cat#SML0430
Ni-NTA Superflow	Qiagen	Cat#30410
Peptide CEP55 ZF (435-464) V438W (CEP55 ZF (W) WT)	Covalab (Villeurbane, France)	N/A
Peptide CEP55 ZF (435-464) V438W/E460A (CEP55 ZF (W) E460A)	Covalab (Villeurbane, France)	N/A
Peptide Strep-tag-II CEP55 ZF WT (435-464) (st-II CEP55 ZF WT)	Covalab (Villeurbane, France)	N/A
Peptide Strep-tag-II CEP55 ZF E460A (435-464) (st-II CEP55 ZF E460A)	Covalab (Villeurbane, France)	N/A
Peptide Fluoresceine – CEP55 ZF WT (435-464) (F-ZF WT)	Covalab (Villeurbane, France)	N/A

Continued		
REAGENT or RESOURCE	**SOURCE**	**IDENTIFIER**
Peptide Fluoresceine – CEP55 ZF E460A (435-464) (F-ZF E460A	Covalab (Villeurbane, France)	N/A
Strep-tag-II	Covalab (Villeurbane, France)	N/A
Proteinase K	EMD Millipore	Cat#70663
mono-ubiquitin	Boston Biochem	Cat#U-100H
Biotinylated Lys-63 Ub2-7	Boston Biochem	Cat#UCB-330
Biotinylated Lys-K48 Ub2-7	Boston Biochem	Cat#UCB-230
K11 tetra-ub	Lifesensor	Cat#SI-1104-0025
Critical Commercial Assays		
PureLink™ HiPure Plasmid Filter Maxiprep Kit	Invitrogen	Cat#K210016
Experimental Models: Cell Lines		
HeLa	ATCC	CCL-2
U-2 OS	LONZA	Scholefield et al. 2016
FreeStyle™ 293-F cells	ThermoFisher scientific	Cat#R79007
Experimental Models: Organisms/Strains		
E. coli BL21-Gold (DE3) Competent Cells	Agilent Technologies	Cat#230132
E. coli XL1-Blue Competent Cells	Agilent Technologies	Cat#200249
Oligonucleotides		
CEP55 siRNA (CAGGTTATTGCTAATGGGTTA)	Qiagen	Cat#SI02653021
Non-targeting siRNA (sequence not provided)	Dharmacon	Cat#D-001810-10
CEP55 gRNA (sequence not provided)	Santa Cruz Biotechnology	Cat#417522
Recombinant DNA		
pET28 CEP55 WT His-NOA (304-396)	This Study/GeneART (ThermoFisher scientific)	N/A
pET28 CEP55 Δ(343-364) His-NOA	This Study/GeneART (ThermoFisher scientific)	N/A

Continued

REAGENT or RESOURCE	SOURCE	IDENTIFIER
pET28 CEP55 L351A/Q354A/Q355A His-NOA	This Study/GeneART (ThermoFisher scientific)	N/A
pET28 CEP55 D362R/F363P His-NOA	This Study/GeneART (ThermoFisher scientific)	N/A
pcDNA3 HA-CEP55 WT (1-464)	This Study/Invitrogen	N/A
pcDNA3 HA-CEP55 D362R/F363P (1-464)	This Study/Invitrogen	N/A
pcDNA3 HA-CEP55 C440A/C443A (1-464)	This Study/Invitrogen	N/A
pcDNA3 HA-CEP55 E460A (1-464)	This Study/Invitrogen	N/A
pGEX4T2-di-Ub (GST)	Ngadjuea et al. 2013	N/A
pGEX4T2-tetra-Ub (GST)	Ngadjuea et al. 2013	N/A
pcDNA3 His-strep-CEP55 WT (1-464)	This Study/Eurofins Genomics	N/A
pcDNA3 His-strep-CEP55 C440A/C443A	This Study/Eurofins Genomics	N/A
pcDNA3 His-strep-CEP55 ΔZF-UBZ^{WRNIP1}(15-53)	This Study/Eurofins Genomics	N/A
pcDNA3 His-strep-CEP55 ΔZF-UBZ^{RAD18} (201-240)	This Study/Eurofins Genomics	N/A
pcDNA3 His-strep-CEP55 ΔZF-UBZ^{NDP52}(440-470)	This Study/Eurofins Genomics	N/A
pcDNA3 His-strep-CEP55 ΔZF-nZF2^{TAB2} (665-693)	This Study/Eurofins Genomics	N/A
pcDNA3 His-strep-CEP55 ΔZF-A20^{ZF7}(759-790)	This Study/Eurofins Genomics	N/A
pEGFP-C1 GFP-ZF^{CEP55}	This Study/Eurofins Genomics	N/A
pET52b3C/LIC Strep-Tag-II- E2–25K-C170S	Merck Millipore	N/A
pGEX-Ubc13 (GST)	Raasi et al., 2015	Addgene plasmid #18894
pET16b- His- Mms2	Raasi et al., 2015	Addgene plasmid #18893

Continued		
REAGENT or RESOURCE	**SOURCE**	**IDENTIFIER**
pET28 His-Darpin 1D5	Wyler et al., 2007	N/A
Software and Algorithms		
SWISS-MODEL worksplace	Arnold et al., 2006	https://swissmodel.expasy.org/
PROCHECK	Laskowski et al., 1993	N/A
GROMOS96	Van Gunsteren et al., 1996	N/A
HADDOCK	De Vries et al., 2010	https://haddock.science.uu.nl/
Kaleidagraph	Synergy software	version: 4.5.2
Icy	De Chaumont et al., 2012	http://icy.bioimageanalysis.org/
Data Analysis BLItz version 1.2 (Fortebio)	Fortebio	https://www.fortebio.com/software-updates.html
ASTRA VI	Wyatt technology	version: 6.0.2
REAGENT or RESOURCE	**SOURCE**	**IDENTIFIER**
Others		
anti-GST biosensors	Fortebio	18-5096
SA-streptavidin biosensors	Fortebio	18-5019
Penta-His biosensors	Fortebio	18-5077